Stiffness-dependent active wetting enables optimal collective cell durotaxis

Macià-Esteve Pallarès[1†], Irina Pi-Jaumà[2,3†], Isabela Corina Fortunato[1], Valeria Grazu[4,5,6], Manuel Gómez-González[1], Pere Roca-Cusachs[1,7], Jesus M de la Fuente[4,5,6], Ricard Alert[8,9]*, Raimon Sunyer[1,7,10]*, Jaume Casademunt[2,3]*, Xavier Trepat[1,6,7,11]*

[1]*Institute for Bioengineering of Catalonia (IBEC), The Barcelona Institute for Science and Technology (BIST) 08028 Barcelona, Spain.*
[2]*Departament de Física de la Matèria Condensada, Universitat de Barcelona, 08028 Barcelona, Spain.*
[3]*Universitat de Barcelona Institute of Complex Systems (UBICS), 08028 Barcelona, Spain.*
[4]*Instituto de Nanociencia y Materiales de Aragón (INMA), CSIC-Universidad de Zaragoza, Zaragoza 50009, Spain.*
[5]*Consejo Superior de Investigaciones Científicas, 50018 Zaragoza, Spain.*
[6]*Centro de Investigación Biomédica en Red de Bioingeniería (CIBER-BBN), 08028 Barcelona, Spain.*
[7]*Departament de Biomedicina, Universitat de Barcelona, 08036 Barcelona, Spain.*
[8]*Max Planck Institute for the Physics of Complex Systems, 01187 Dresden, Germany.*
[9]*Center for Systems Biology Dresden, 01307 Dresden, Germany.*
[10]*Institute of Nanoscience and Nanotechnology (IN_2UB), 08010 Universitat de Barcelona, Barcelona, Spain.*
[11]*Institució Catalana de Recerca i Estudis Avançats (ICREA), 08010 Barcelona, Spain.*

[†] *These authors contributed equally to this work.*

* Correspondence to:

Xavier Trepat, PhD
Institute for Bioengineering of Catalonia
Ed. Hèlix, Baldiri i Reixac, 15-21, 08028 Barcelona, Spain
Email: xtrepat@ibecbarcelona.eu

Jaume Casademunt, PhD
Facultat de Física, Universitat de Barcelona
Av. Diagonal, 647, 08028 Barcelona, Spain
Email: jaume.casademunt@ub.edu

Raimon Sunyer, PhD
Facultat de Medicina, Universitat de Barcelona
Casanova 143, 08036 Barcelona, Spain
Email: rsunyer@ub.edu

Ricard Alert, PhD
Max Planck Institute for the Physics of Complex Systems
Nöthnitzerst. 38, 01187 Dresden, Germany
Email: ralert@pks.mpg.de

Abstract

The directed migration of cellular clusters enables morphogenesis, wound healing, and collective cancer invasion. Gradients of substrate stiffness are known to direct the migration of cellular clusters in a process called collective durotaxis, but underlying mechanisms remain unclear. Here, we unveil a connection between collective durotaxis and the wetting properties of cellular clusters. We show that clusters of cancer cells dewet soft substrates and wet stiff ones. At intermediate stiffness, at the crossover from low to high wettability, clusters on uniform-stiffness substrates become maximally motile, and clusters on stiffness gradients exhibit optimal durotaxis. Durotactic velocity increases with cluster size, stiffness gradient, and actomyosin activity. We demonstrate this behavior on substrates coated with the cell-cell adhesion protein E-cadherin and then establish its generality on substrates coated with extracellular matrix. We develop a physical model of three-dimensional active wetting that explains this mode of collective durotaxis in terms of a balance between in-plane active traction and tissue contractility, and out-of-plane surface tension. Finally, we show that the distribution of cluster displacements has a heavy tail, with infrequent but large cellular hops that contribute to durotactic migration. Our study demonstrates a physical mechanism of collective durotaxis, through both cell-cell and cell-substrate adhesion ligands, based on the wetting properties of active droplets.

Introduction

The ability of cells to migrate following gradients of environmental properties drives numerous biological processes in health and disease[1]. Cells undergo directed migration in response to gradients of chemical factors[2], electric fields[3], and mechanical properties of their microenvironment[4–7]. This latter process, called durotaxis, has been implicated in morphogenesis[8,9], wound healing[10] and cancer invasion[11].

Durotaxis was originally discovered as the directed migration of single cells following a gradient in the stiffness of an underlying substrate[4]. Later on, cell collectives were found to perform durotaxis much more efficiently than single cells[12,13]. Collective durotaxis has now been established *in vitro* as the asymmetric spreading of an epithelial monolayer[12,13] and *in vivo* as the key mechanism driving the cohesive migration of the neural crest cluster during development of *Xenopus laevis*[9]. Despite the growing recognition of the physiological relevance of durotaxis in development and disease, underlying mechanisms remain poorly understood. This limitation arises, in part, from the lack of data on how durotaxis depends on key physical variables of the motile cluster, such as its size, adhesion, three-dimensional shape, and active forces. Moreover, current theoretical models[12,14–21] do not integrate all these physical variables into a physical framework that explains collective durotaxis.

Durotaxis of single cells and clusters has so far been studied in the presence of gradients in the stiffness of the extracellular matrix (ECM)[4–7,12,22,23]. However, important migratory processes during development and cancer progression take place in contexts lacking ECM[24,25]. This is illustrated by border cell migration during *Drosophila* oogenesis, which is mediated by E-cadherin-based adhesion between the migratory cluster and surrounding stationary cells[25,26]. Other examples of cell migration through cadherin adhesion include zebrafish primordial germ cells[27], mouse retinal endothelial cells[28], and mouse neuronal precursors[29]. Cadherin-based migration is also likely to play a role in epithelial tumors in which collective invasion and remodeling are predominantly governed by cell-cell adhesion rather than by the ECM[30]. Although collective migration through cadherin receptors is well established, whether these cell-cell adhesion proteins can mediate durotaxis is unknown.

Here we provide a systematic mechanical analysis of collective durotaxis in three-dimensional epithelial clusters. We begin studying durotaxis on substrates coated with E-cadherin. We show that clusters of human epidermal carcinoma cells (A431) display low motility on the soft and stiff regions of the substrate, where they fully dewet and wet the surface, respectively. At intermediate stiffness, close to the crossover between low and high wettability, cell clusters are maximally motile on uniform-stiffness substrates and exhibit optimal durotaxis on stiffness gradients. We develop a continuum model of three-dimensional active wetting that explains this non-monotonic durotactic behavior in terms of a balance between cellular traction, contractility and surface tension. Cell clusters then perform cohesive

durotactic migration as their interface advances on the stiff side and retracts from the soft side. We show that this physical mechanism applies not only to surfaces coated with cell-cell adhesion ligands but also with cell-ECM ligands as long as clusters are brought close to the crossover between low and high wettability, which we call the neutral wetting regime.

Results

Cell clusters become most motile at their neutral wetting regime

We first studied the spontaneous migration of cell clusters (83±54 cells/cluster, mean + SD, Extended Data Fig. 1a) on polyacrylamide gels of uniform stiffness (0.2, 6, 24 and 200 kPa) functionalized with oriented E-cadherin extracellular domains (Fig. 1; Extended Data Fig. 2). Using a custom-made tracking algorithm, we measured the cluster position for 14h at 10 min intervals (Fig. 1a-c; Supplementary video 1). The dependence of cluster velocity with stiffness was non-monotonic; it was minimal at low stiffness (0.2 kPa), peaked at intermediate stiffness (24 kPa), and then decreased at high stiffness (200 kPa) (Fig. 1b,d). This non-monotonic behavior coincided with different regimes of cluster spreading, which we interpret within the conceptual framework of tissue wetting[14,15,31–38]. At low stiffness, clusters were nearly spherical and the contact angle (θ) between the cluster and the substrate was close to 180º, indicating full dewetting (i.e. complete retraction) (Fig. 1a,e,f). By contrast, at high stiffness, clusters spread to form a monolayered epithelium with a low contact angle, indicating full wetting (i.e. complete spreading). At intermediate stiffness, for contact angles around 90º, clusters displayed highly dynamic protrusions (Fig. 1f; Supplementary video 1,2). To characterize these protrusions, we imaged clusters transfected with mCherry-Lifeact at high spatial and temporal resolution. The resulting movies revealed that these protrusions are dynamic filopodia (Supplementary video 3), in which actin flows retrogradely towards the cluster core (Supplementary video 4). Taken together, these data suggest that at the crossover between low and high wettability ($\theta \sim 90°$), which we define as the neutral wetting regime, clusters become maximally motile by rapidly engaging and disengaging actin-rich protrusions with the substrate.

We next examined whether these local protrusions generated traction forces. We performed 3D Traction Force Microscopy (TFM) experiments on clusters seeded on polyacrylamide gels of 1 and 6 kPa in stiffness (Fig. 1g-j). At higher stiffness, TFM showed insufficient resolution to robustly measure the three traction components. We characterized traction profiles through their radial component (T_r), defined as the component perpendicular to the cluster edge in the substrate plane, and through the normal component to the substrate (T_z). Both on 1 kPa and 6 kPa substrates, radial tractions pointed towards the center of the cluster (Fig. 1g-i). Normal tractions were positive near the cluster edges and became negative towards the cluster center. These data reveal a cluster surface tension (γ) that pulls the cluster edge upwards at the contact line with the substrate. Consistent with this picture, cell protrusions

at the cluster edge were not parallel to the substrate but rather formed acute angles with it (Fig. 1f; Extended Data Fig. 3). Upwards traction at the cluster edge is balanced by a pressure that pushes the cluster core into the substrate. Whereas the spatial profiles of T_z and T_r displayed qualitative similarities on 1 kPa and 6 kPa, the magnitude of both components increased with stiffness, indicating that in-plane tractions and surface tension are mechanosensitive[39–42] (Fig. 1i,j).

Cell clusters exhibit durotaxis on E-cadherin substrates

The highly dynamic state of epithelial clusters in the neutral wetting regime led us to hypothesize that they might be particularly responsive to gradients in substrate stiffness. To test this hypothesis, we fabricated substrates exhibiting stiffness gradients[43] and functionalized them with the oriented extracellular domain of E-cadherin at uniform density (see Methods and Extended Data Fig. 4). As in previous experiments, we tracked the migration of cell clusters for 14h at 10 min intervals (Fig. 2a; Supplementary videos 5,6). After each experiment, we measured the substrate stiffness profile with Atomic Force Microscopy (AFM). Using this approach, we built a large dataset matching the local mechanical properties of the substrate with the instantaneous velocity of each cluster. Clusters migrating on stiffness gradients showed a significantly positive velocity (v_X) along the direction of the gradient, indicating durotaxis towards increasing stiffness (Fig. 2b). This biased migration was also evident when comparing the angular distribution of cluster trajectories for uniform (Fig. 2c) and gradient (Fig. 2d) gels. These experiments show that durotaxis is not restricted to integrin-mediated migration on ECM substrates. Rather, the cell migration machinery can also drive durotactic responses through cadherin receptors.

Durotaxis depends on stiffness, stiffness gradient, cluster size and cell contractility

We next explored whether durotaxis depends on local substrate stiffness (E). As in the case of substrates of uniform stiffness, clusters dewetted regions of low stiffness and wetted those of high stiffness (Fig. 2a; Supplementary video 5). In these two extreme cases, the cluster durotactic velocity v_X was low (Fig. 2e). However, in regions of intermediate stiffness, clusters were in the neutral wetting regime and durotaxis peaked. Thus, as in uniform substrates (Fig. 1d), cluster velocity was maximal at intermediate stiffness, but in this case migration was directed towards higher stiffness rather than random.

To characterize durotaxis, we studied the role of cluster size, cell contractility, and stiffness gradient. We found that large clusters (diameter >60 μm) were more durotactic than smaller ones (Fig. 2e), and their velocity peaked at higher stiffness (Fig. 2e). To decrease cell contractility, we treated cells with a low dose (0.5 μM) of the ROCK inhibitor Y-27632. As expected, for any given stiffness this treatment resulted systematically in smaller contact angles (Extended Data Fig. 1b). We also found that the decrease in contractility reduces durotaxis and shifts the durotaxis peak to lower stiffness compared to untreated clusters (Fig. 2f; Supplementary video 7). Finally, to study how durotaxis depends on the

stiffness gradient, we generated substrates with low, middle, and high steepness. Since durotaxis varies with local stiffness, we measured cluster velocity on each gradient substrate at a similar starting stiffness (18 ± 5 kPa). We found a significant increase in durotaxis with the stiffness gradient (Fig. 2g). Together, these results establish that durotaxis is optimal in the neutral wetting regime and depends on cluster size, contractility, and stiffness gradient.

A three-dimensional model of active wetting explains non-monotonic tissue durotaxis

So far, our data show that the peaks in cluster velocity and durotaxis correlate with the wetting state of the cell clusters. To understand how the tissue wetting properties might lead to collective durotaxis, we model clusters as active fluid droplets that partially wet the substrate. Accordingly, we describe a cluster as a spherical cap of radius R_{sphere}, whose contact surface with the substrate is a circular cell monolayer of radius R (Fig. 3a). Based on the observation that protrusive activity is largely restricted to cells in contact with the substrate (Extended Data Fig. 3, Supplementary Videos 2-4), we assume that the dynamics of the droplet is controlled by the in-plane forces in the basal monolayer, which we model as a 2D active polar fluid, extending previous work[14,15,31,38,44]. The cells at the periphery of this monolayer are polarized outwards and exert two types of active forces (Fig. 3a, inset): cell-substrate traction with a maximum value ζ_i, which promotes tissue spreading, and cell-cell contractility with magnitude $\zeta < 0$, which promotes tissue retraction. This cell-cell contractility refers to active contractile stresses within and between cells, generated by the actomyosin cytoskeleton and transmitted across the cell monolayer through cell-cell junctions. Previous work showed that the competition between traction and contractility in this 2D model gives rise to an active wetting transition between monolayer spreading (wetting) and retraction (dewetting)[14,31,38].

Here, we extend the theory of active wetting to 3D droplets (Supplementary Note). We propose a generalized Young-Dupré force balance between the active forces in the basal monolayer and the out-of-plane surface tension γ of the cell cluster, defining a contact angle θ (Fig. 3a). The horizontal component of the surface tension, $-\gamma \cos\theta$, combines with the monolayer active forces to drive either spreading or retraction, damped by both monolayer viscosity η and substrate friction ξ. For sufficiently large surface tension, the tissue may reach a stable equilibrium with a static contact angle defining partial wetting with high ($\theta < 90°$) or low ($\theta > 90°$) wettability (Supplementary Note). In turn, the vertical component of surface tension is balanced by the Young-Laplace pressure $P = 2\gamma/R_{\mathrm{sphere}}$ exerted on the contact surface (Fig. 3a). Assuming that the surface tension, and hence the Laplace pressure, is uniform across a cluster, we use this relation to infer the value of γ in our experiments from measured vertical traction forces (Fig. 1g-j), which provide a direct measurement of P (see Table 2 in Methods).

To capture collective durotaxis, we take into account that cellular forces depend on substrate stiffness. Following previous work[14,45–50], we assume that both the active traction ζ_i and the friction coefficient ξ increase and saturate with the substrate's Young modulus E. This is consistent with our measurements, which show that radial in-plane tractions increase with substrate stiffness (Fig. 1g-i). In addition, our measurements reveal that out-of-plane tractions also increase with stiffness (Fig. 1j), implying that the tissue surface tension features an active mechanosensitive response[51,52]. Consistently, we assume that the pressure P is an increasing function of E, which we take as linear for simplicity. Altogether,

$$\zeta_i(E) = \zeta_i^{\infty} \frac{E}{E + E^*}, \quad \xi(E) = \xi^{\infty} \frac{E}{E + E^*}, \quad P(E) = P_0 + s_P E, \tag{1}$$

where ζ_i^{∞} and ξ^{∞} are saturation values, E^* is a characteristic stiffness of force saturation, P_0 is the bare pressure, and s_P is the pressure sensitivity to stiffness.

With this model, we simulate the motion of a cluster up a stiffness gradient $E(x) = E_0 + E'x$ (Fig. 3b). As the cluster moves to stiffer regions, its contact angle decreases (Fig. 3c, brown), but its durotactic velocity varies non-monotonically (Fig. 3c, red), in agreement with our experimental measurements (Fig. 2e,f). We explain the origin of this non-monotonic behavior below.

Irrespective of the wettability of the 3D droplet, the balance of in-plane forces at the basal monolayer yields two basic predictions. First, as predicted in Refs.[14,15], the durotactic velocity v_X increases with the difference between the active traction at the front (stiff edge) and at the rear (soft edge) of the cluster (Supplementary Note). Hence, v_X increases with the stiffness gradient, consistently with our measurements (Fig. 2g). Second, at high stiffness, active traction forces saturate. Hence, the active traction difference across the cluster decreases, which results in slower durotaxis (Fig. 3d). In parallel, the friction coefficient increases (and also saturates) with stiffness, which also results in slower durotaxis (Supplementary Note). This slowdown was also observed in our experimental measurements (Fig. 2e,f), and it can arise either at $E > E^*$ due to traction saturation or at $E < E^*$ due to increasing friction (Fig. 3d).

However, our experiments also show that the durotactic velocity increases with stiffness in the low stiffness area of the substrate (Fig. 2e,f). This increase could be explained by the fact that the stiffness gradient generated by our fabrication method increases in this region of the substrate (Extended Data Fig. 4a). To test this possibility, we took advantage of the gel-to-gel variability (Extended Data Fig. 4b) and, for each stiffness bin, we restricted our analysis to the data points with a gradient of 40±10 kPa/mm. We found that in these conditions of nearly constant gradient, the non-monotonic behavior of durotactic velocity with stiffness was retained (Extended Data Fig. 5). This result indicates that the sharp increase in durotactic velocity in the low stiffness region of the gel cannot be attributed to changes in the stiffness gradient.

Instead, using our 3D active wetting theory, we predict that this feature arises from the wettability of the tissue, i.e. the contact angle θ determined by the generalized Young-Dupré force balance (Supplementary Note). As in our experiments (Fig. 1e,f), at low stiffness the tissue has high contact angles ($\theta > 90°$, Fig. 3b,c). As a result, the contact radius R is small. This leads to a small active traction difference across the tissue, and hence a small durotactic velocity. However, the contact angle is large, and therefore surface tension pulls the cluster edges out (Fig. 3a, left) and gives rise to a positive spreading velocity (Fig. 3c, blue). As a result, the contact angle decreases (Fig. 3c, brown), consistent with experiments (Fig. 1e,f), and the durotactic velocity increases (Fig. 3c, red). The speedup of durotaxis at low stiffness is thus favored by surface tension. Increasing it by increasing the pressure sensitivity to stiffness s_P indeed yields smaller contact angles and hence faster durotaxis (Fig. 3e). The positive feedback between spreading and durotaxis produces a fast growth of the durotactic velocity, up to the regions where the surface tension contribution changes sign, at the contact angle of 90º (Fig. 3a, middle). After this point, surface tension points inwards and no longer promotes spreading (Fig. 3a, right); the spreading velocity therefore decreases (Fig. 3c, blue), and durotaxis slows down. Altogether, the combined effects of three-dimensional active wetting and the saturation of cellular forces at high stiffness explain why the durotactic velocity first increases and then decreases with substrate stiffness, as observed in our experiments (Fig. 2e,f), with a maximum around the contact angle of 90º (Fig. 3c).

The dependence of durotaxis on cluster size, cellular contractility, and stiffness gradient is also captured by our model. First, larger clusters have a larger active traction difference across them, which produces a higher durotactic velocity and shifts its maximum towards higher substrate stiffness (Fig. 3f), as in our experimental results (Fig. 2e). Second, the ROCK inhibitor Y-27632 reduces myosin-generated cellular contractility, which we implement by reducing the magnitude of all active forces in the model: monolayer contractility ζ, active traction ζ_i, and tissue surface tension γ. Both contractility and active traction are active forces that would vanish completely with no myosin activity. In contrast, surface tension also has a passive contribution from cell-cell adhesion[53], which produces a significant tissue surface tension even without myosin activity. Accordingly, we decrease contractility and active traction by a larger factor than surface tension. These parameter changes allow us to recover the decrease of durotactic velocity and the shift of its maximum towards lower stiffness (Fig. 3g) observed in our experimental results (Fig. 2f). Finally, increasing the stiffness gradient in the model produces faster durotaxis (Fig. 3h), which is consistent with our experimental measurements (Fig. 2g).

All in all, our model shows how the interplay between cell contractility, cluster size, stiffness, and cell traction forces can position clusters near contact angles of $\theta = 90º$, and thus provide them with the sweet spot where cluster durotaxis is maximal.

Cell clusters also durotax on ECM ligands close to neutral wetting

According to our theory, the emergence of fast durotaxis in the neutral wetting regime should be independent of the nature of the adhesion ligand. We thus tested whether a similar phenomenology can be observed on ECM ligands rather than on E-cadherin. Cell clusters were seeded on polyacrylamide gels of 0.2, 6, 24 and 200 kPa functionalized with fibronectin. Clusters displayed higher wettability on fibronectin than on E-cadherin substrates, fully wetting the substrates except for the lowest stiffness (Fig. 4a). To push the neutral wetting regime to an intermediate stiffness range, we treated clusters with 10 ng/mL of human Epidermal Growth Factor (hEGF), which increases cell contractility[54,55] and cluster surface tension (Extended Data Fig. 6). With this treatment, cluster morphology showed a dependence with stiffness similar to that observed on E-cadherin substrates; full dewetting on soft substrates and a crossover to high wettability at intermediate stiffness (Fig. 4a,b). Cluster velocity was maximum in this intermediate regime, displaying a non-monotonic relationship with stiffness similar to that observed on E-cadherin substrates (Fig. 4c; Supplementary video 8). We then asked whether hEGF-treated clusters display durotaxis on substrates with a stiffness gradient coated with fibronectin. We found that this was indeed the case (Fig. 4d,e; Supplementary video 9). Like for cadherin-coated substrates, durotaxis was non-monotonic and peaked at the neutral wetting regime (Fig. 4f). Taken together, these data demonstrate that the durotaxis mode observed on E-cadherin gels is not a unique feature of cell-cell adhesion ligands. Rather, our data support that this behavior is a generic feature of clusters at the crossover between low and high wettability, whose location is tuned by substrate properties and active forces.

Sudden detachments of protrusions give rise to long durotactic hops

Finally, we studied the statistics of cell cluster movements. To this end, we computed the probability distribution of the displacements (ρ) of clusters on stiffness gradients coated with E-cadherin (Fig. 5). We found that most displacements were well described by an exponential distribution (Fig. 5a), as previously shown during random migration of single cells[56,57]. However, this distribution fails to capture long displacements (> 25 μm), which are much more frequent than expected. This fat tail in the distribution, which accounts for 0.4% of the total displacements, corresponds to hops that result from sudden retraction of cluster protrusions (Fig. 5b; Supplementary video 10). Strikingly, we found that these large hops are more durotactic than small displacements (Fig. 5c,d). Thus, cluster durotaxis arises from a combination of frequent small displacements and rare large hops.

Discussion

Collective durotaxis is increasingly recognized as a key mechanism to drive directed cell migration in development[8,9] and disease[1,11]. In this study, we provided a systematic analysis of collective durotaxis as a function of the physical properties of the cluster (size, three-dimensional shape, contractility) and

of the substrate (stiffness, stiffness gradient, ligand identity). The analysis of hundreds of clusters revealed that durotaxis is a non-monotonic function of local substrate stiffness with a peak at intermediate stiffness. We showed that the position of the peak can be shifted to higher or lower stiffness by tuning cluster size and active forces. We developed a 3D model that captures the phenomenology in terms of the physics of active wetting.

As predicted in previous theoretical work[14,15], our results experimentally demonstrate a mode of durotaxis in which cell clusters move as a whole, with the front and rear edges displacing in the same direction. This behavior is different from early studies of collective durotaxis using flat monolayers, which showed asymmetric spreading rather than directed migration[12,13]. Moreover, we generalize the theory of active wetting[31] to 3D clusters including tissue surface tension to account for partial wettability, i.e. finite contact angles. We show that the interplay between wettability and substrate stiffness is essential to explain the non-monotonic behavior of durotaxis. This wetting-based mode of durotaxis may involve but does not require long-range force transmission across the tissue. This feature distinguishes it from previous models of durotaxis that imposed global force transmission by treating the cell cluster as an elastic medium[12,16,58–60]. Overall, our work provides a theory for stiffness-dependent 3D active wetting that explains the measured properties of collective cell durotaxis, and may serve as a guide for further experiments. These experiments should seek to understand, for example, whether the width of the peak can be tuned as predicted by the model, which we were unable to analyze in this work due to high scattering of the data. In the future, the picture reported here can be extended to account for flows resulting from spatial pressure variations across a cluster, for the size-dependent surface tension of cell aggregates[61], and for elastocapillary effects resulting from substrate deformation[62–64].

Our study demonstrates that durotaxis can be mediated not only by ECM ligands but also by E-cadherin. E-cadherin migration is relevant in early developmental stages in which the ECM is absent or weakly expressed. The paradigmatic example of collective cell migration through cadherin receptors is border cell migration during *Drosophila* oogenesis[25,26]. In this process, the cohesive border cell cluster migrates antero-posteriorly in the egg chamber by establishing dynamic protrusions with neighboring nurse cells through E-cadherin receptors. In zebrafish, E-cadherin also mediates the migration of progenitor cells and of cell sheets during epiboly[65,66]. In cancers that retain epithelial features, E-cadherin is the dominant adhesion molecule between cancer cells and is therefore responsible for local and global migratory events and rearrangements within the tumor[30,67]. Besides E-cadherin, N-cadherin has also been shown to mediate long distance migration of inter-neuron precursors and neurite outgrowth[29,68,69]. In all these processes, the mechanisms driving directed cell migration remain incompletely understood. Whereas determining the presence of mechanical gradients *in vivo* presents outstanding experimental challenges, our results establish durotaxis as a plausible mechanism underlying directed cell migration based on cadherin adhesion.

We studied whether the existence of optimal cluster durotaxis in the neutral wetting regime is independent of the nature of the adhesion ligand by carrying out experiments on substrates coated with E-cadherin and fibronectin. Clusters on E-cadherin exhibited full dewetting on all substrates except for the stiffest ones. By contrast, clusters on fibronectin fully wetted all substrates except for the softest ones. Several molecular mechanisms could explain these differences. These include differences in coating density, in affinity of cadherin-cadherin vs fibronectin-integrin bonds[70], in adhesion reinforcement mechanisms[71] (e.g. talin vs alpha-catenin unfolding), in lateral adhesion clustering[72] or in adhesion regulation by growth factors[73]. Irrespective of the molecular mechanisms at play, an increase in contractility with hEGF brought clusters on fibronectin-coated substrates to wettability conditions similar to those on cadherin-coated substrates, showing full dewetting on soft substrates, full wetting on stiff ones, and neutral wetting at intermediate stiffness. Under these conditions, the non-monotonic behavior of durotaxis was recovered, indicating that this behavior is independent of the nature of the adhesion ligand.

Inspection of the distribution of cluster displacements showed that collective durotaxis involves a combination of small but frequent displacements following an exponential distribution and large but rare hops following a power law. Dynamics featuring rare and sudden reconfiguration events have been described in disordered systems including rearrangements in colloidal glasses, avalanches in sandpiles, and earthquakes in geological systems[74,75]. These apparently distinct materials, which span several orders of magnitude in size, share that they all respond to slow shear through some kind of stick-slip dynamics[76]. The data presented here suggest that these dynamics also take place in wetting processes in tissues, enabling the emergence of fast directed migration.

Our finding of an optimal regime for collective durotaxis provides a new strategy for the regulation of directed cell migration *in vivo*. By tuning the local stiffness of a substrate or the active properties of a cluster, organisms can finely control the onset of directed migration and its extent[77]. Conversely, abnormal tissue stiffening or softening, or changes in active cluster mechanics could impair physiological migration or trigger undesired durotaxis. A particularly relevant pathological context for our findings concerns the movement of cellular clusters during cancer invasion and metastasis. Our results indicate that these clusters will exhibit poor migration when fully wetting or dewetting their microenvironment, but will be able to follow stiffness gradients efficiently at the crossover between low and high wettability. Further work is needed to study the wettability of cellular clusters *in vivo* and the implications in physiological and pathological directed cell migration. Our study provides a general physical framework to address this question.

Acknowledgments

We thank all the members of our groups for their discussions and support. We thank Anghara Menéndez, Susana Usieto and Beatriz Martin for technical assistance and Anabel-Lise Le Roux for helping to produce and purify histidine-tagged mCherry. We also thank Erik Sahai for sharing cell lines and plasmids used in this work. Finally, we thank Juan Francisco Abenza, Eleni Dalaka and Tom Golde for their feedback on the manuscript. This paper was funded by the Generalitat de Catalunya (AGAUR SGR-2017-01602 to X.T., AGAUR SGR-2017-1061 to J.C., the CERCA Programme, and "ICREA Academia" awards to P.R-C. and J.C.); Spanish Ministry for Science and Innovation MICCINN/FEDER (PGC2018-099645-B-I00 to X.T., PID2019-110298GB-I00 to P.R-C., PID2019-108842GB-C21 to J.C., RTI2018-101256-J-I00 and RYC2019-026721-I to R.S., FPU19/05492 to I.P-J., FPU15/06516 to M-E.P.); Fondo Social de la DGA (grupos DGA) to V.G. and J.M.F.; European Research Council (Adv-883739 to X.T.); Fundació la Marató de TV3 (project 201903-30-31-32 to X.T.); European Commission (H2020-FETPROACT-01-2016-731957 to P.R-C. and X.T.); the European Union's Horizon 2020 research and innovation programme (under the Marie Skłodowska-Curie grant agreement no. 797621 to M.G-G.); La Caixa Foundation (LCF/PR/HR20/52400004 to to P.R-C. and X.T.); IBEC is recipient of a Severo Ochoa Award of Excellence from the MINECO. R.S. is a Serra Húnter fellow.

Author contributions

M-E.P., R.S. and X.T. conceived the project. M-E.P., R.S., and I.C.F. performed experiments. V.G., J.M.F. and P.R-C. contributed technical expertise, materials and discussion. I.P-J., R.A. and J.C. developed the model. M.G-G. and R.S. developed analysis software. M-E.P., I.P-J., R.A., R.S., J.C., and X.T. wrote the manuscript. All authors revised the completed manuscript. R.A., R.S., J.C. and X.T. supervised the project.

Competing interests

The authors declare no competing financial interests

Code availability

Analysis procedures and code implementing the model are available from the corresponding authors on reasonable request.

Data availability

The data that support the findings of this study are available from the corresponding authors on reasonable request.

Extended Data is available for this paper

Correspondence and requests for materials should be addressed to R.A., R.S., J.C. or X.T.

Methods

Cell culture

A431 cells were cultured in Dulbecco's Modified Eagle's Medium containing high glucose and pyruvate (11995, Thermofisher) supplemented with 10% fetal bovine serum, 100 units·ml^{-1} penicillin and 100 µg·ml^{-1} streptomycin. Cells were maintained at 37ºC in a humidified atmosphere containing 5% CO_2. Prior to experiments, cells were starved for 24 hours in starvation media (Dulbecco's Modified Eagle's Medium containing high glucose and pyruvate supplemented with 1% FBS, 100 units·ml^{-1} penicillin and 100 µg·ml^{-1} streptomycin). Versene (15040066, Gibco) was used to collect cells from flasks as a non-enzymatic cell dissociation reagent aiming to preserve the integrity of membranal E-cadherin molecules prior to cell seeding on gels functionalized with E-cadherin.

Cell clusters formation

A431 heterogeneous cell clusters were obtained by seeding $5 \cdot 10^3$ cells/well in Corning Costar Ultra-Low Attachment Multiple Well Plate (CLS3474-24EA) in starvation media. Cell clusters were mechanically disaggregated into smaller clusters exhibiting heterogeneous sizes by pipetting up and down with a series of pipette tips of different sizes. Cellular debris was discarded by centrifuging disaggregated clusters at 0.3 rpm for 0.5 min.

Cell clusters seeding

Cell clusters were resuspended in media containing 5 µM RHO/ROCK pathway inhibitor (Y-27362) and seeded on stiffness gradients in a total volume of 50 µL to allow for cluster adhesion to the entire surface of the gradient, thus covering the whole range of stiffness. 45 minutes later, 1 mL of media containing 5µM RHO/ROCK pathway inhibitor (Y-27362) was added to prevent the gels from drying out. After 1 hour, Y-27362 was carefully removed by slow aspiration and 1.5mL of fresh starvation medium was added. Clusters were imaged 2 hours later.

Lentiviral transfection for stable Lifeact-mCherry expression

HEK293T cells were transfected as previously described[78] to produce lentiviral particles inducing stable expression of Lifeact-mCherry. A431 wild type cells were infected as previously described[78]. Two weeks later, infected cells were sorted using an ARIA fluorescence-activated cell sorter (BD) aiming to select those cells exhibiting similar fluorescence intensity.

Cell adhesion assay

A431 cells were resuspended at a concentration of 10^6 cells/mL and incubated for 15min in ice-cold starvation media containing either 40 µg/mL α-GFP antibody (A10262, Life technologies; Control) or 40 µg/mL DECMA-1 antibody (U3254, Sigma Aldrich). Cells incubated with control or DECMA-1

antibody were seeded on gels functionalized with E-cadherin. Cell adhesion was allowed for 15min before gently washing three times with 1xPBS containing calcium and magnesium, and the remaining adhered cells were fixed with 4% PFA in 1xPBS containing calcium and magnesium, followed by Hoecsht staining for nuclei quantification. An inverted microscope (Nikon Eclipse Ti) equipped with a 2x 0.06NA objective was used to image the entire gel surface. An intensity threshold was set on FiJi software to binarize the images and automatically count the number of adhered cells per condition. Cell density was assessed, data sets were transformed to obtain normal distributions and non-parametric statistical tests were performed.

Glass-bottom dish silanization

Glass-bottom dishes (P35-0-20, Mattek) were silanized using a 2:1:80 solution of acetic acid/bind-silane (M6514, Sigma)/ethanol for 30 min. The dishes were washed twice with ethanol and dried by aspiration.

Polyacrylamide gels of uniform stiffness

A 1 mL gel premix solution containing 2% bis-acrylamide and 40% acrylamide (proportions vary according to desired stiffness; see Table 1), 15µL irgacure 5% w/v (BASF, Germany), 6 µL acrylic acid (147230, Sigma Aldrich), 84 µL 1M NaOH and 10 µL 500nm-diameter yellow-green fluorospheres was prepared (F8813, Thermofisher). A drop of 16 µL of gel premix was added to the center of the previously silanized glass-bottom dish, and an 18-mm diameter glass coverslip treated with Repel Silane (General Electric, USA) was placed on top to distribute the volume evenly and flatten the gel surface. Glass-bottom dishes containing a sandwich of gel premix were placed under UV light for 5min to allow for gel polymerization. Next, 10x PBS was added and round-tip tweezers were used to separate top coverslips from the gels polymerized on glass-bottom dishes.

Stiffness (kPa)	**40% Acrylamide (µL)**	**2% Bis-acrylamide (µL)**
0.2	125	32
1	87	33
6	187	70
24	244	125
200	480	187

Table 1. Stiffness and corresponding Acrylamide/Bis-acrylamide concentrations for 1mL gel premix.

Polyacrylamide gels with a stiffness gradient

A 25µL drop of gel premix containing 15% acrylamide, 1% bis-acrylamide, 0.75 $mg \cdot mL^{-1}$ irgacure, 0.60% acrylic acid, 100mM NaOH and a dilution of 1:100 from stock 500nm-diameter fluorescent beads (F8813, Thermofisher) was added to the center of previously silanized glass-bottom dishes and

covered with an 18mm-diameter glass coverslip treated with Repel Silane (General Electric, USA). Gradients of stiffness on polyacrylamide gels were obtained as previously described[12,43]. Briefly, making use of an opaque sliding mask during UV-triggered gel polymerization we polymerized gels exhibiting a gradient of stiffness. To obtain "shallow" and "steep" gradients, the opaque mask was moved at rates of 50 $\mu m \cdot s^{-1}$ and 30 $\mu m \cdot s^{-1}$, respectively. Finally, 10xPBS was added to facilitate the removal of top coverslips using round-tip tweezers. Gel stiffness was measured with AFM after every experiment.

Gel functionalization with oriented E-cadherin

To functionalize uniform and stiffness gradient gels we used a previously described method involving carbodiimide reactions[79]. Briefly, a mix of 20 mM Nα,Nα-Bis(carboxymethyl)-L-lysine hydrate (NTA-NH2, 14580, Sigma-Aldrich) and 25 mM Copper (II) Sulphate 5-hydrate ($CuSO_4$, 131270, Panreac) in 1xPBS buffer was brought to pH=10.0 and centrifuged at 4500 rpm for 15min. The pellet was discarded while the supernatant (formed by a solution containing NTA-NH_2/Cu^{2+} complex) was brought to pH=7 and filtered using a 0.20 μm diameter filter. In parallel, previously polymerized polyacrylamide gels were incubated with 100mM N-(3-dimethylaminopropyl)-N′-ethylcarbodiimide hydrochloride crystalline, imidazole (EDC, E6383, Sigma-Aldrich) and 200mM N-Hydroxysuccinimide (NHS, 130672, Sigma-Aldrich) in 20mM Hepes pH=7.0 buffer at 37ºC for 20min. Then, the gels were quickly washed twice with 1xPBS and incubated at 37ºC with filtered NTA-NH_2/Cu^{2+} solution aiming to bind it covalently to carboxyl groups on the gel surface. Two washes with 1xPBS were performed 45min later, followed by addition of 1M Tris(hydroxymethyl)aminomethane hydrochloride (TRIS, 648317 Merck) pH=8.0 for 30min to hydrolyze unreacted active carboxyl groups. Next, the gels were washed twice with 1xPBS and incubated at room temperature with a drop of 25μL of $0.01 mg \cdot mL^{-1}$ histidine-tagged E-cadherin (8505-EC-050, R&D Systems) covered with rectangles of parafilm, ensuring an even distribution of the drop across the entire surface of the gel. E-cadherin oriented chelation on the gel was achieved after 1 hour of incubation, and excess E-cadherin molecules were rinsed with two washes of 1xPBS. The metal chelation of its C-terminal polyhistidine tail, via the metal chelator complex (NTA-Cu^{2+}) previously introduced at the polyacrylamide gels surface, guarantees the proper orientation of the protein fragment by mimicking its presentation on cell surfaces. However, the polyhistidine-NTA interaction is highly dependent on pH, ionic strength, and other media conditions. Thus, the gels were incubated with 50mM EDC and 75mM NHS in 20mM pH=7.0 Hepes buffer at 37ºC for 45 min aiming to covalently bind E-cadherin molecules to the gels by promoting amide link formation between amino groups in the polihistidine tag and the carboxylated groups presented in the NTA. Next, the gels were washed twice with 1xPBS and incubated with 1M imidazole/1mM EDTA in PBS for 20min to compete for/chelate copper ions and thus rinse non-covalently bound E-cadherin molecules, followed by two

1xPBS washes. Finally, the gels were passivated with 0.1 $mg \cdot mL^{-1}$ pLL-g-PEG, sterilized with UV and used for experimental purposes within the 24h after the functionalization process.

Gel functionalization with fibronectin

Polyacrylamide gels were functionalized using carbodiimide reactions. Briefly, gels were incubated with 100 mM EDC and 200 mM NHS in 20 mM Hepes pH=7.0 buffer at 37ºC for 20 min. Next, gels were quickly washed twice with 1xPBS and incubated at 37ºC with a dilution of 0.1 mg/mL fibronectin (33016015) in 1xPBS for 45 min. Finally, gels were washed twice with 1xPBS and incubated with 1M Tris pH=8.0 for 30 min at RT, followed by two 1xPBS washes. Gels were kept overnight at 4ºC prior to UV-sterilization and cluster seeding.

Histidine-tagged GFP and histidine-tagged mCherry production and purification

Histidine-tagged GFP and histidine-tagged mCherry were produced in *Rosetta E. coli* strain and purified using Ni-NTA columns, as previously described[80].

Protein incorporation quantification in polyacrylamide gels

To study the protocol's functionalization efficiency, histidine-tagged E-cadherin was replaced by Histidine-tagged GFP, whose functionalization and orientation are achieved likewise, offering a direct fluorescence readout for the protocol validation. Aiming to provide a realistic idea of the extent of protein incorporation, their molar concentrations were normalized. Fluorescence images were taken from functionalized gels using an inverted microscope (Nikon Eclipse Ti) equipped with a 10x 0.30 NA objective (for stiffness gradient gels) or a 20x 0.45 NA objective (for uniform stiffness gels).

Further experiments were carried out to assess the functionalization protocol in a stepwise manner. Polyacrylamide gels depleted of acrylic acid were not functionalized with histidine-tagged GFP molecules, indicated by a decay in fluorescence intensity. A second round of EDC/NHS activation was carried out aiming at the formation of a covalent bond between histidine-tagged GFP molecules and the gel. The decay in fluorescence intensity after imidazole-mediated rinse in gels that did not undergo a second round of EDC/NHS activation suggested that histidine-tagged GFP orientation was achieved as a result of histidine chelation of histidine-tagged GFP molecules by NTA/Cu^{2+} complexes. Maximum fluorescence intensity values were obtained after a second round of EDC/NHS activation in gels that were not rinsed with imidazole/EDTA. A mild decay of fluorescence intensity experienced by an imidazole/EDTA-mediated rinse in gels that underwent a second round of EDC/NHS activation suggested that a significant part of histidine-tagged GFP molecules were successfully oriented and covalently bound to the gels after the second round of EDC/NHS activation (Extended Data Fig. 2b).

Contractility enhancement and inhibition experiments

To study the effect of contractility on cluster migration, 0.5 μM Y-27632 ROCK inhibitor and 1.65 nM human epidermal growth factor (hEGF) were used to inhibit and enhance cell contractility, respectively.

Time lapse microscopy

Multidimensional acquisition routines were performed on automated inverted microscopes (Nikon Eclipse Ti) equipped with thermal, CO_2 and humidity control using MetaMorph, Micromanager and NIS-Elements softwares. Time-lapse experiments started approximately 4h after cell seeding. The image acquisition interval was set to 10 min, and a typical experiment was run for at least 14h. Images were acquired using a 10x 0.3 NA objective, and an automated stage was used to save 3 overlapping stage positions that covered ~3 mm of the stiffness gradients starting from the soft edge.

High-resolution images of cell clusters

An inverted Nikon microscope equipped with a spinning disk confocal box (CSU-WD, Yokogawa) was used to acquire high resolution images of A431 mCherry-Lifeact cell clusters seeded at different stiffness. A z-step equal to 0.2 μm was acquired for every cluster, ensuring to capture whole cell clusters.

Contact angle measurement

To compute the contact angle (θ) formed between the substrate and the line tangent to the edge of the cluster (Fig. 1e, inset) we acquired high resolution stacks of mCherry-Lifeact A431 cell clusters seeded on 0.2, 1, 6, 24 and 200 kPa (the *z*-step was 0.26 μm after correcting for the focal plane shift). Extended Data Fig. 7 shows the basic strategy used to calculate the contact angle as a function of the cluster radius (R_{sphere}), the contact radius (R) and the cluster height (H). In dewet clusters, we estimated R_{sphere} from the maximum Z projection of all the images in the stack and R from the basal plane (Extended Data Fig. 7a). Then, the contact angle was given by $\theta = 180 - \mathrm{asin}\left(\frac{R}{R_{\mathrm{sphere}}}\right)$. For wet clusters, we estimated R_{sphere} from the height H and R (Extended Data Fig. 7b). Both H and R were measured from the Z stack. Then, the contact angle was given by $\theta = \mathrm{asin}\left(\frac{R}{R_{\mathrm{sphere}}}\right)$.

Traction force microscopy

Traction forces were computed using Fourier transform based traction microscopy with a finite gel thickness as previously described[81]. Gel displacements experienced between any experimental timepoint and a reference image of the relaxed state of beads after cell cluster trypsinization were computed using home-made particle imaging velocimetry software[81].

Stiffness gradient profile measurement with Atomic Force Microscopy

Stiffness gradients and uniform stiffness gels were mapped individually using a commercial Atomic Force Microscope (AFM) (JPK Nanowizard) operated as previously described[82,83]. Briefly, a V-shaped cantilever (Bruker) with a triangular tip and a spring constant of k = 0.03 N·m^{-1} was used to indent the gels to ensure the cantilever deflection resulted within the linear detection range of the AFM. The cantilever spring constant was calibrated using a thermal fluctuation method. The relationship between the photodiode signal and cantilever deflection was computed from the slope of the force displacement curve obtained at a region without gel sample. For each sample, 5 force-displacement (F-z) curves (where $F = k \cdot d$, d being the deflection and z being the piezotranslator position) were acquired by ramping the cantilever forward and backward at a constant speed (5 μm amplitude, 1 Hz and approximately 1 μm of indentation). Each experimental F-z curve was fitted to the four-sided pyramidal indenter model:

$$F = \frac{E \cdot \tan\theta}{2^{\frac{1}{2}} \cdot (1 - \nu^2)} \cdot \delta^2, \quad (2)$$

where E is the Young's modulus, ν is the Poisson's ratio, θ is the semi-included angle of the pyramidal indenter and δ is the indentation depth. The parameter ν is assumed to be 0.5, and the indentation depth is calculated as $\delta = z - z_0 - d$, where z_0 is the tip-gel contact point. E and z_0 were estimated by least-squares fitting of this equation to the F-z curve recorded on each gel point. Young's modulus was measured every 200 μm along the axis of maximum gel stiffness change.

Cluster tracking using phase images

Custom-made Matlab scripts combined with "Grid/Collection stitching" plug-in from FiJi software were used in order to register and stitch three overlapping images covering 3 mm of the stiffness gradients. Briefly, time-lapse images from the green fluorescent channel containing fluorescent beads (F8812, ThermoFisher) were registered using a custom-made Matlab script. "Grid/Collection stitching" plugin from FiJi was used to stitch registered maximum intensity images from fluorescent beads, and a custom-made Matlab script was run in order to stitch phase contrast images using the XY coordinates provided by FiJi.

Stitched phase contrast images were used to segment clusters. Images were treated with gaussian and standard deviation filters to find cluster edges. After applying automatic thresholding and detection algorithms we detected cluster position. Clusters were linked based on proximity, and tracks were generated and labelled with sequential numbers. Segmented images with cluster labels were merged with phase contrast images, and clusters were manually selected using the label number. Inconsistently tracked and incorrectly segmented clusters were discarded for analysis. Clusters whose tracks left the field of view were kept until the timepoint in which their outline overlapped with the image boundary,

whereas clusters whose tracks interacted were kept until the timepoint in which the interaction took place. Final tracks contained the *x* and *y* position for each cluster at the measured timepoints. Noise in trajectories was estimated at 1.5 μm by tracking pieces of immobile debris.

Image processing of high-resolution images of clusters

Acquired images of mCherry-Lifeact A431 cell clusters were processed using Imaris software. A gaussian filter was applied to the images to smoothen the fluorescence signal before generating a surface to visualize the tridimensional shape of clusters.

Statistics

Statistical analyses and plotting were performed using R v 4.1.2 (R Core Team). For comparing two groups, we performed two-sample permutation t-test implemented in the "MKinfer" library. We assessed differences among groups using permutation-based analysis of variance (Permutation-based ANOVA), which does not require normality or homogeneity of variances, using the "lmperm" library. We ran a post hoc permutational test to assess the pairwise significance among groups, using the library "rcompanion" and reporting the adjusted p-value with the "false discovery rate" method. 95% confidence intervals of medians were estimated using bootstrap intervals of 10,000 resamples.

Modelling dynamic evolutions

We assume that a spherical-cap cluster evolves while keeping the total volume fixed. The stiffness profile is chosen to be linear with position on the gel (Eq. (S15)) with its values inferred from experiments (Fig. 2a as a representative example). Traction, friction, and surface tension functions with the stiffness are chosen, linear (for simplicity, following Eqs. (S16)-(S18)) or saturated (Eq. (S12)). At each step, the velocity profile is computed solving Eq. (S6), with the polarity profile Eq. (S7) and the boundary conditions Eq. (S11). By a simple Euler integration algorithm with a time step Δt, the center-of-mass X and contact radius R are evolved following

$$R(t+\Delta t) = \frac{1}{2}\big(x_+(t+\Delta t) - x_-(t+\Delta t)\big) = \frac{1}{2}\big(x_+(t) + v\big(x_+(t)\big)\Delta t - x_-(t) - v\big(x_-(t)\big)\Delta t\big) = R(t) + v_S(t)\Delta t, \quad (3)$$

$$X(t+\Delta t) = \frac{1}{2}\big(x_+(t+\Delta t) + x_-(t+\Delta t)\big) = \frac{1}{2}\big(x_+(t) + v\big(x_+(t)\big)\Delta t + x_-(t) + v\big(x_-(t)\big)\Delta t\big) = X(t) + v_X(t)\Delta t. \quad (4)$$

Imposing volume conservation with $V_{\text{const}} = \frac{\pi}{6}H(H^2 + 3R^2)$, this fixes the new height, and then the contact angle is

$$\theta = \begin{cases} 180 - \operatorname{asin}\left(\dfrac{R}{R_{\text{sphere}}}\right) \geq 90°, & H \geq R \\ \operatorname{asin}\left(\dfrac{R}{R_{\text{sphere}}}\right) \leq 90°, & H \leq R \end{cases} \quad (5)$$

In general, the clusters do not strictly follow a quasistatic evolution, defined as a sequence of stages with vanishing spreading velocity (see for instance v_S in Fig. 3c and Figs. S9-S11).

Model parameters fit

We use the experimental measures from Table 2 as references to infer the dependencies of the active traction parameter ζ_i and pressure P with stiffness, since $\zeta_i \sim T_r/h$ (where h is the height of the basal monolayer, typically $h = 5$ μm[31,81]) and $P \sim T_z$. Through Laplace's law, surface tension is $\gamma = \frac{PR_{\text{sphere}}}{2}$ and so it will depend on the size of the clusters. From here, the slopes of these profiles might be slightly changed to explore a wider range of the phenomenology from the model. Typically, we take $\zeta_i^{\infty} = 0.3$ kPa/μm[31,44], a range of $E^* = (50 - 450)$ kPa for the active traction saturation profile (Eq. (S12)), and a range of pressure sensitivity to stiffness of $s_P = (0.3 - 9.1) \times 10^{-2}$ for the linear pressure increase (Eq. (S13)).

Stiffness (kPa)	**Traction T_r (Pa)**	**Traction T_z (Pa)**	**Surface tension γ (mN/m)**
1	10	10	0.15
6	40	50	0.75

Table 2. Approximate experimental measures of the radial T_r and vertical T_z components of traction forces in cell clusters on top of uniform-stiffness substrates of 1 and 6 kPa (from Fig. 1i,j). Also, surface tension estimates for clusters of an apparent size of $R_{\text{sphere}} \sim 30$ μm (Fig. 1g,h).

Main figures and legends

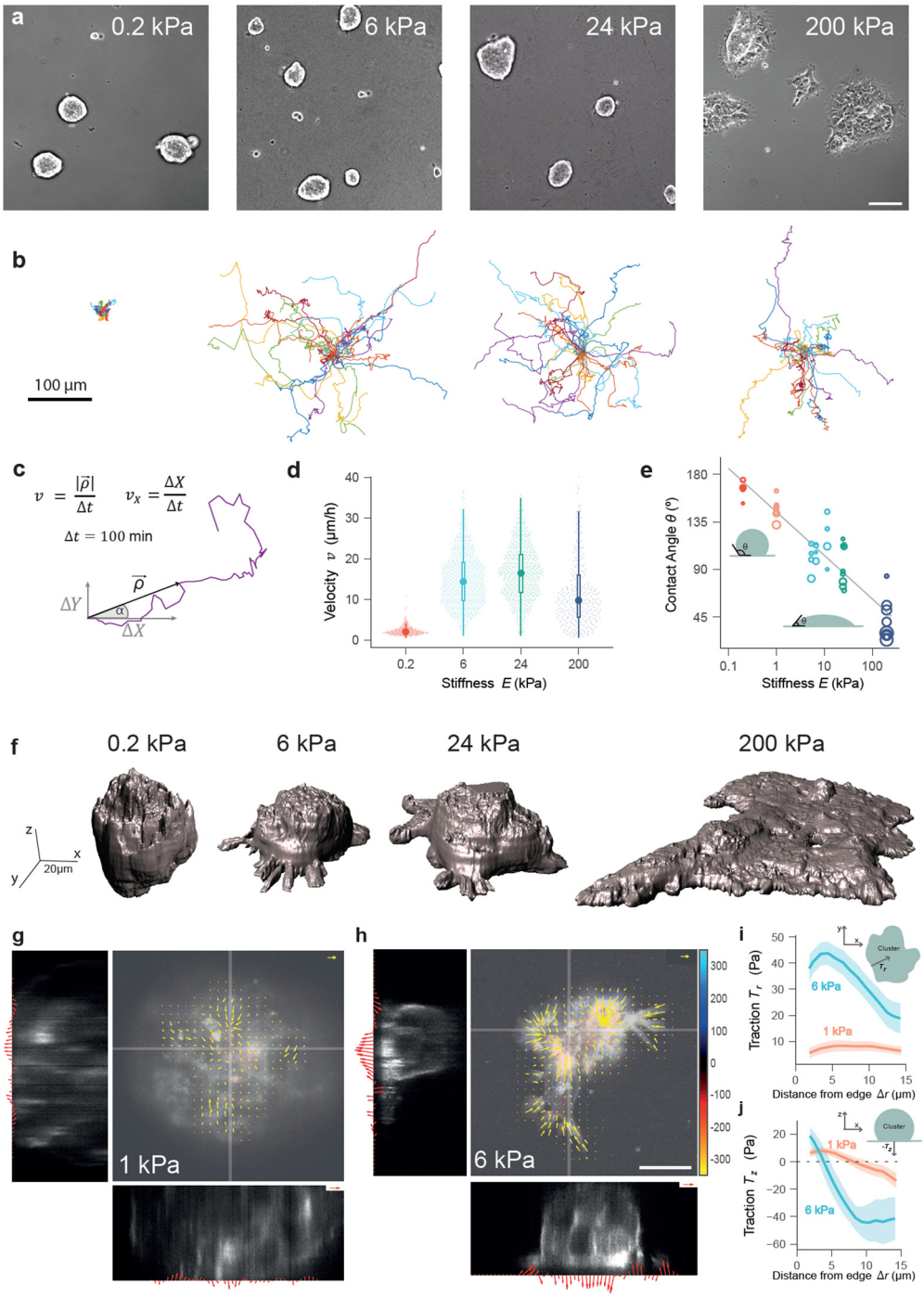

Figure 1. **Epithelial cell clusters on E-cadherin-coated substrates show optimal motility in the neutral wetting regime. a**, Representative phase contrast images of A431 cell clusters seeded on E-cadherin-coated gels of uniform stiffness of 0.2, 6, 24 and 200 kPa. Scale bar, 100 µm. **b**, Representative trajectories of clusters migrating on the E-cadherin-coated gels shown in panel (a). **c**, Scheme representing the workflow to track cluster trajectories and velocity. Velocity was computed at 100 min intervals. **d**, Cluster velocity at different substrate stiffness. Small dots represent individual clusters. The central dot in front of the boxplot represents the median. For the sake of visualization, clusters above the percentile 99.5% are not represented. Permutation tests (two

tailed) were performed, in which significant differences were observed across all combinations (p-values < 0.0001). n= 296 clusters (0.2 kPa), n= 646 clusters (6 kPa), n= 561clusters (24 kPa), n= 266 clusters (200 kPa). **e**, Contact angle θ between the cell cluster and the substrate for different substrate stiffness. Each dot is the averaged contact angle for one cluster. Circle size is proportional to cluster average diameter. n= 43 clusters. **f**, 3D rendering of representative clusters on substrates of different stiffness. **g-h**, Traction forces exerted by representative clusters on 1 and 6 kPa E-cadherin-coated gels. Yellow vectors represent traction forces in the *xy*-plane while red vectors represent traction forces projected on the corresponding lateral planes (*xz* and *yz*) along the gray lines shown in the central panels (reference vectors are 50 Pa, scale bar is 25 μm). **i**, Mean of the radial component of the traction force in the *xy*-plane for 1 kPa (n= 35 clusters) and 6 kPa gels (n= 19 clusters) as a function of distance from the cluster edge. **j**, Mean of the vertical component of the traction force for 1 kPa (n= 13 clusters) and 6 kPa gels (n= 7 clusters) as a function of distance from the cluster edge. Shaded areas in i-j represent 95% confidence interval (CI).

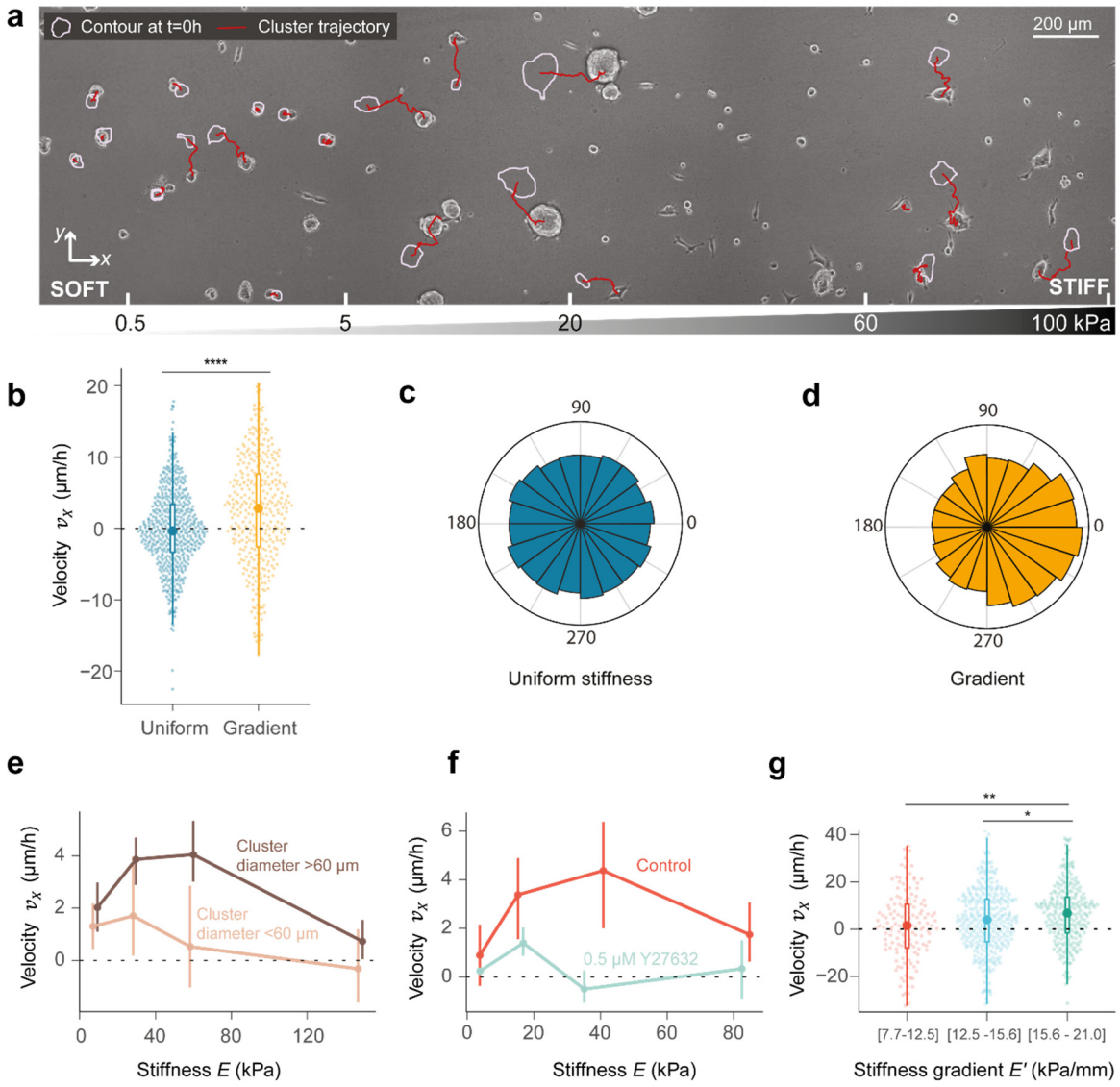

Figure 2. **Collective durotaxis is optimal in the neutral wetting regime. a**, Representative phase-contrast image of A431 cell clusters migrating on a stiffness gradient coated with E-cadherin. Image was taken at 10h. The original position (0h) of each cluster is represented by a purple outline. The red line represents the trajectory obtained by time-lapse microscopy. The bottom scale indicates the stiffness at each point of the image. **b**, Cluster velocity v_X along the direction of the gradient on uniform (6 kPa) and gradient stiffness gels. Small dots represent individual clusters. The central dot in front of the boxplot represents the median. (Permutation t-test (two tailed), $p < 0.0001$). n= 527 clusters (Uniform), n= 366 clusters (Gradient, data pooled from all regions of the substrate). **c-d**, Distribution of the angle α between the instantaneous velocity vector and the x-axis (see Fig. 1c) for uniform stiffness gels (c) and stiffness gradients (d). **e**, Durotactic velocity as a function of stiffness. Light brown labels small clusters (diameter < 60 µm), whereas dark brown labels large clusters (diameter > 60 µm). Vertical bars indicate 95% CI. Bin 1 ($0 < E \leq 20$ kPa): diameter < 60 µm, n=72 clusters (529 displacements); diameter > 60 µm, n=90 clusters (584 displacements). Bin 2 ($20 < E \leq 40$ kPa): diameter < 60 µm, n=30 clusters (136 displacements); diameter > 60 µm, n=86 clusters (549 displacements). Bin 3 ($40 < E \leq 80$ kPa): diameter < 60 µm, n=37 clusters (205 displacements); diameter > 60 µm, n=106 clusters (629 displacements). Bin 4 ($E > 80$ kPa): diameter < 60 µm, n=53 clusters (248 displacements); diameter > 60 µm, n=186 clusters (1103 displacements). **f**, Durotactic velocity in control clusters (red) and in clusters treated with Y27632 (0.5 µM, light blue). Data includes only clusters > 60 µm. Vertical bars represent 95% CI. Bin 1 ($0 < E \leq 10$ kPa): control, n=11

clusters (82 displacements); 0.5 μM Y27632, n=28 clusters (216 displacements). Bin 2 ($10 < E \leq 25$ kPa): control: n=19 clusters (105 displacements); 0.5 μM Y27632, n=29 clusters (164 displacements). Bin 3 ($25 < E \leq 60$ kPa): control, n=14 clusters (77 displacements); 0.5 μM Y27632, n=11 clusters (69 displacements). Bin 4 ($E > 60$ kPa): control, n=13 clusters (71 displacements); 0.5 μM Y27632, n=18 clusters (70 displacements). **g**, Durotactic velocity for different stiffness gradients for a fixed starting stiffness E=18 ± 5 kPa. Clusters on steeper gradients showed significantly more durotaxis than those on milder ones (Permutation test, p-values: Bin 1 vs Bin 2, 0.1014; Bin 2 vs Bin 3, 0.0463; Bin 1 vs Bin 3, 0.0026). Each point represents a displacement. The central dot in front of the boxplot represents the median. For the sake of visualization, clusters above the percentile 99.5% are not represented. Bin 1 ($7.7 < E' \leq 12.5$ kPa/mm): n=20 clusters (141 displacements); Bin 2 ($12.5 < E' \leq 15.6$ kPa/mm): n=45 clusters (339 displacements); Bin 3 ($15.6 < E' \leq 21$ kPa/mm): n=41 clusters (248 displacements).

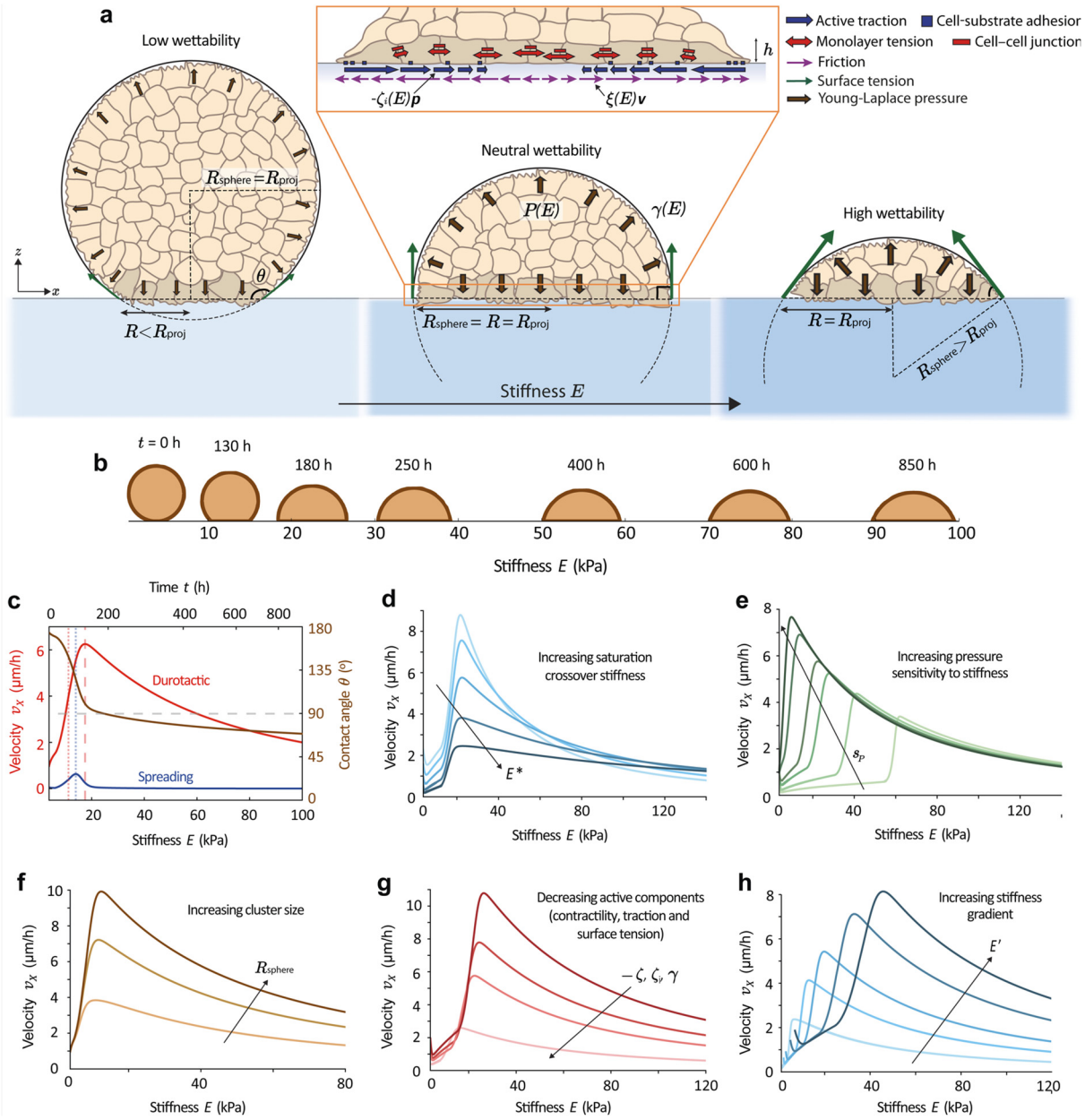

Figure 3. **A three-dimensional model of active wetting explains non-monotonic tissue durotaxis. a**, Scheme of the model for a cell cluster on substrates of different stiffness E. R_{proj} is the projected radius of the cell cluster, which is the radius measured in phase-contrast images. The inset shows a zoom-in of the basal cell monolayer (represented with darker cells for visualization) with schematic representations of the cell-substrate forces and the monolayer tension. In all panels **b-h**, the initial contact radius is $R_0 = 3.0$ μm and height $H_0 = 56.8$ μm (giving a contact angle of $\theta_0 = 174°$ and volume $V = 92500\pi/3$ μm^3), and the initial substrate stiffness is $E_0 = 3.8$ kPa. Except for the parameters that we are changing in each panel, other parameter values are listed in Table SI, with a simulation time-step of $\Delta t = 6$ min. See simulation details in the Methods section. **b-c,** Representative example of the velocity and shape dynamics of a migrating cluster with a constant volume, showing the snapshots of the cluster shape (**b**) and the non-monotonic dependence of the durotactic velocity v_X with stiffness (in red), the spreading velocity (in blue) and the decrease of the contact angle (in brown) (**c**). Since the cluster migrates towards stiffer regions of the substrate, the stiffness and time axes run in parallel. In this case, we have taken a saturating pressure profile with stiffness to study how the angle keeps decreasing at large stiffness, with $P^{\infty} = 0.6$ kPa and $E_P^* = 10$ kPa and following the same expressions than in Eq. (S12). **d,** The saturation crossover stiffness E^* controls the decrease of velocity at high stiffness as it tunes both friction and active traction increase and saturation with stiffness. Here, $E^* = 50, 80, 140, 260, 450$ kPa from lighter to darker blue. **e**, The increase of surface

tension, and hence pressure, with stiffness controls the increase of velocity at low stiffness. Here, $P' = (0.1, 0.2, 0.4, 0.6, 1.5, 3.0)$ Pa/μm, which corresponds to $s_P = (0.3, 0.6, 1.2, 1.8, 4.5, 9.1) \cdot 10^{-2}$, from lighter to darker green. **f,** Larger clusters are more durotactic and feature the velocity peak at higher stiffness. Here, the initial sizes are $R_{\text{sphere}} = 13.2, 28.5, 61.4$ μm (from lighter to darker brown), giving volumes of $V = \frac{9250\pi}{3}$, $\frac{92500\pi}{3}$, $\frac{925000\pi}{3}$ μm^3, and $\gamma(E) = 0.05 + 0.03(E - E_0)/E'$ mN/m for all sizes. **g,** Clusters with reduced active forces present a lower durotactic velocity with its peak shifted to lower stiffness. Here, contractility and traction are multiplied by factors $\alpha_\zeta = \alpha_{\zeta_i} = 0.4, 1, 1.4, 2$, and surface tension by $\alpha_\gamma = 0.7, 1, 1.2, 1.5$ (smaller factors towards lighter red). **h,** Larger stiffness gradients produce an increase of durotactic velocity and a displacement of its peak towards stiffer regions. Here, $E' = 10, 20, 30, 50, 70$ kPa/mm (from lighter to darker blue).

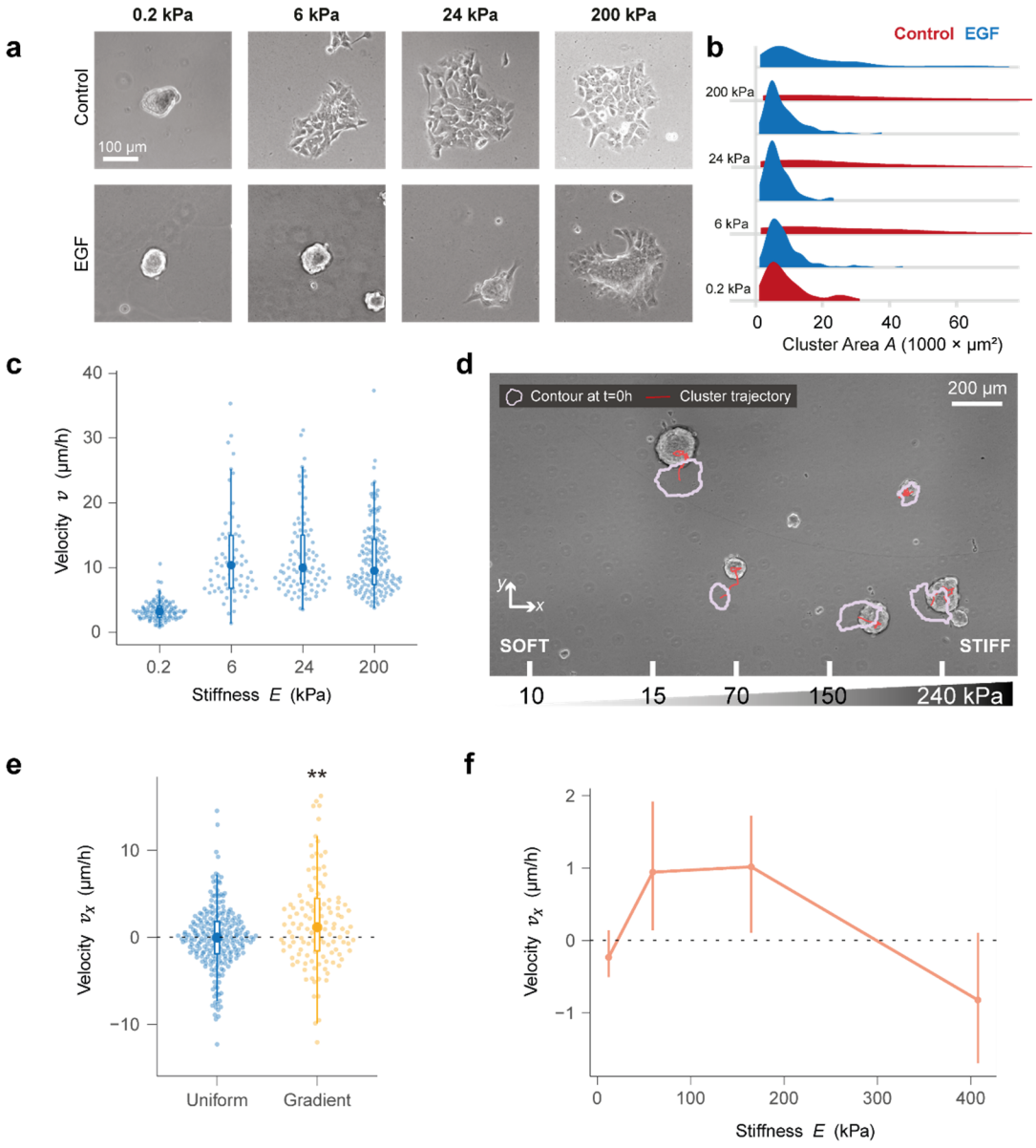

Figure 4: **Wetting-based durotaxis also occurs on ECM substrates at high contractility**. **a**, Representative phase-contrast images of A431 cell clusters seeded on fibronectin-coated uniform-stiffness gels of 0.2, 6, 24 and 200 kPa. **b**, Cluster area distribution for control and 10 ng/ml hEGF treatment. Clusters treated with hEGF spread less at lower stiffnesses than control clusters. **c**, Velocity of hEGF-treated A431 cell clusters on substrates of different stiffness. Velocity was computed at 100 min intervals. Each dot represents a cluster. For the sake of visualization, points above 99.5% percentile are not displayed. n=109 clusters (0.2 kPa), n=68 clusters (6 kPa), n= 89 clusters (24 kPa), n= 157 clusters (200 kPa). **d**, Representative image of hEGF-treated A431 cell clusters migrating on a fibronectin-coated substrate with a stiffness gradient. Image was taken at 10h. The original position (0h) of each cluster is represented by a purple outline. The red line represents the trajectory obtained by time-lapse microscopy. Bottom scale indicates the local stiffness at each point of the substrate. **e**, Velocity along the *x*-axis of hEGF-treated A431 cell clusters, represented by dots, on uniform stiffness gels (pooled data from 0.2, 6, 24 and 200 kPa gels, n=245 clusters) and on stiffness gradients (n=128 clusters). Small dots represent individual clusters. The central dot in front of the boxplot represents the median. For the sake of visualization, points above 98% percentile are not displayed. (Permutation t-test (two tailed), p = 0.0027). **f**, Durotactic velocity as a function of stiffness. Data is median ± 95% CI estimated by bootstrapping; Bin 1 ($0 < E \leq 35$ kPa): n=105 clusters (686 displacements). Bin 2 ($35 < E \leq 100$ kPa): n=50 clusters (310 displacements). Bin 3 ($100 < E \leq 250$ kPa): n=86 clusters (438 displacements). Bin 4 ($E > 250$ kPa): n=46 clusters (222 displacements).

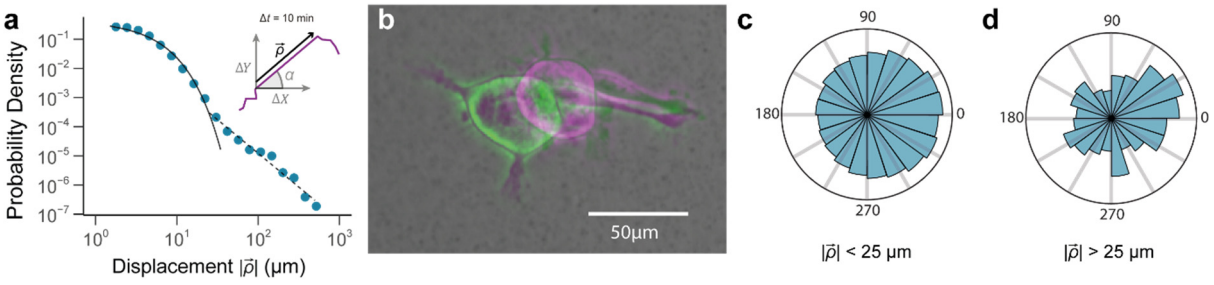

Figure 5. Sudden protrusion detachments give rise to long durotactic hops. a, Probability density of the displacements ρ (see inset) undergone by migrating cell clusters on stiffness gradient gels. Above displacements of 25 μm, the probability distribution deviates from an exponential (solid line) and is captured by a power-law function with exponent -2.31±0.14 (dashed line). Accordingly, we defined displacements $\rho > 25$ μm as long hops. **b**, Example of a sudden detachment of filopodia-like structures that results in a long hop. Green cluster is the initial image and the magenta one depicts the same cluster 10 min later. **c-d**, Distribution of the angle α between the instantaneous velocity vector and the x-axis (see inset of panel **a**) for short (**c**) and long hops (**d**).

Extended Data

Extended data figures

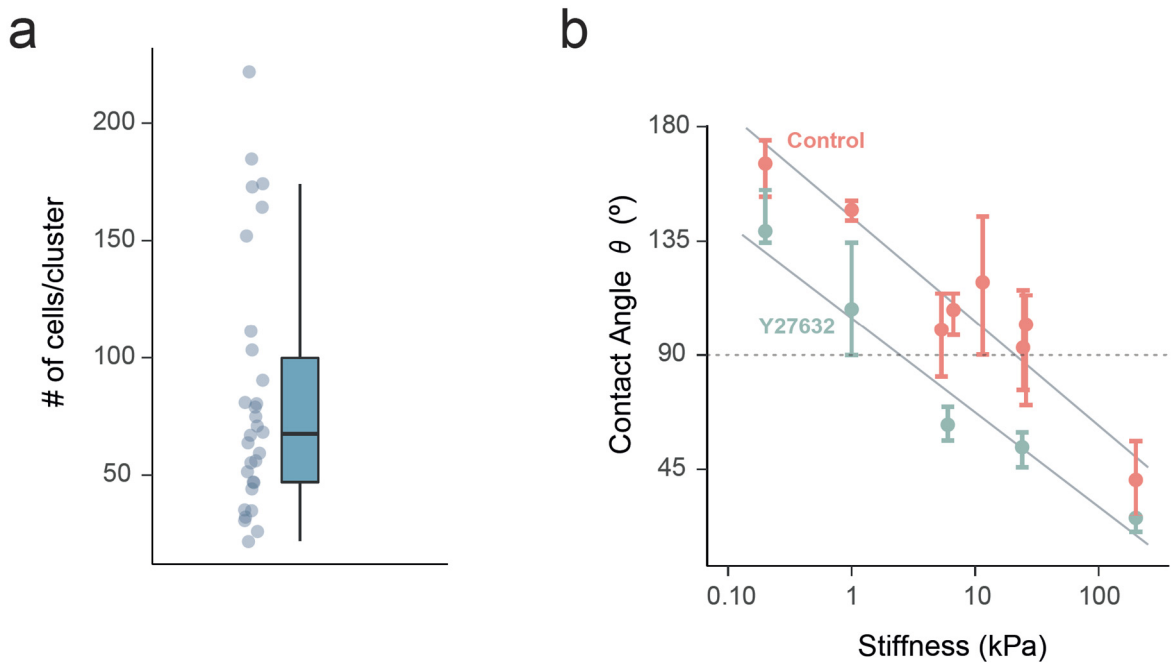

Extended Data Figure 1 | Characterization of cluster size and contact angle. a, Distribution of the number of cells per cluster (n=30 clusters). The high variability was intended in order to study the effect of cluster size on durotaxis. **b,** Contact angle as a function of stiffness for control cells (red) and for cells treated with 0.5 µg/ml of Y27632 (turquoise). Data are median ± 95% CI estimated by bootstrapping (n=4-9 clusters for control and n=8-34 clusters for Y27632).

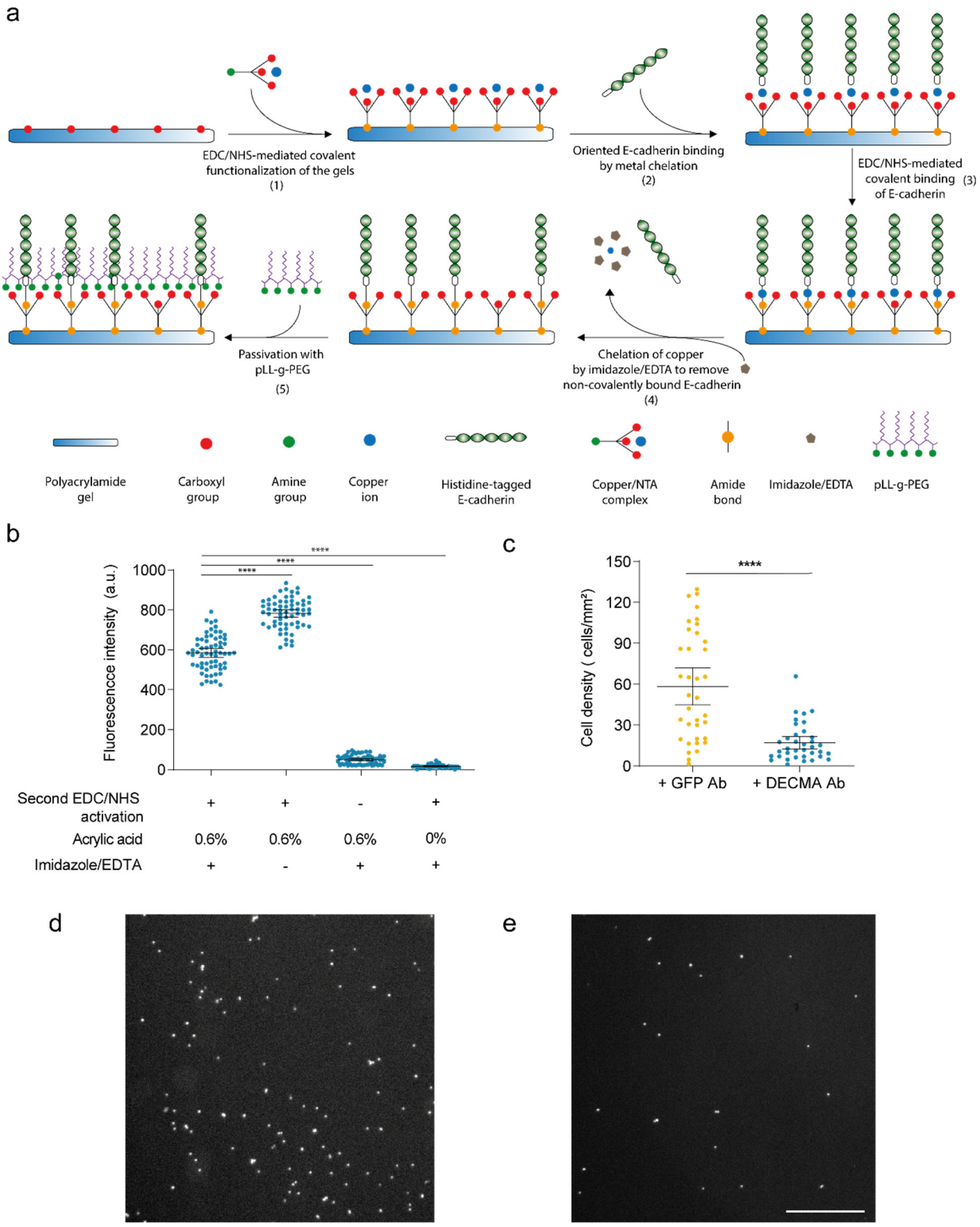

Extended Data Figure 2 | Functionalization of polyacrylamide gels with oriented E-cadherin extracellular domains (EC1-5). a, Scheme showing the protocol to covalently attach E-cadherin extracellular domains on the surface of a polyacrylamide gel mimicking its oriented presentation on cell surfaces. Briefly, polyacrylamide gels containing acrylic acid and thus presenting free carboxyl groups were activated with EDC/NHS and incubated with a solution of NTA/Cu^{2+} complexes (1) aiming to form a covalent amide bond between carboxyl groups in the gels and amino groups from NTA/Cu^{2+} complexes. Next, gels were incubated with histidine-tagged E-

cadherin extracellular domains EC1-5 (2), which spontaneously oriented along NTA/Cu^{2+} complexes through metal chelation of their poly-histidine tag. A covalent amide bond between histidine-tagged E-cadherin extracellular domains and NTA/Cu^{2+} complexes was formed upon a second round of EDC/NHS activation (3). Finally, a solution containing imidazole/EDTA was used to rinse/elute non-covalently bound histidine-tagged E-cadherin extracellular domains (4) prior to gel passivation with pLL-g-PEG (5). **b**, Fluorescence intensity as a readout of protein incorporation in polyacrylamide gels including (+) or omitting (–) steps in the protocol. First row indicates whether gels underwent a second EDC/NHS treatment to covalently bind histidine-tagged GFP to the gels; second row indicates concentration of acrylic acid; third row indicates whether gels were rinsed with imidazole/EDTA to remove non-covalently bound histidine-tagged GFP. **c**, Adhesion assay performed on A431 cells in the presence of E-Cadherin blocking antibody (DECMA). This assay validates the specificity of our coating. For panels b-c, data is mean ± 95% CI. ****, p-value < 0.0001, Permutation test. **d-e**, Fluorescence image of nuclei (labelled with Hoechst) of attached A431 single cells in controls and DECMA-treated A431 single cells, respectively. Scale bar, 500 μm.

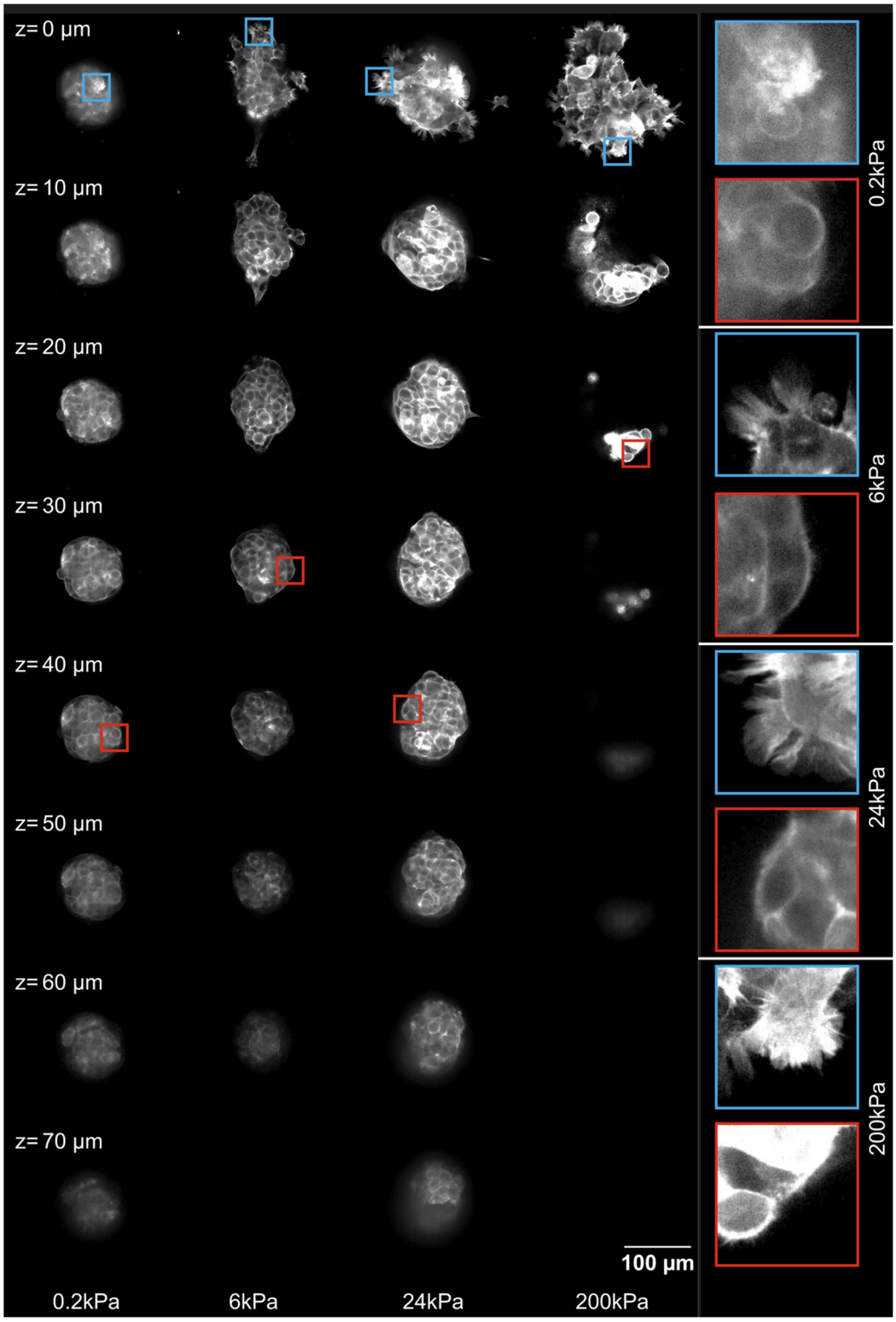

Extended Data Figure 3 | 3D cluster profile. Z-stack of A431 clusters expressing LifeAct-mCherry for 0.2, 6, 24 and 200 kPa uniform stiffness gels coated with oriented E-cadherin. Slices are shown with a z-step size of 10 µm. Basal plane is z = 0 µm. Insets indicate zoomed areas of different planes.

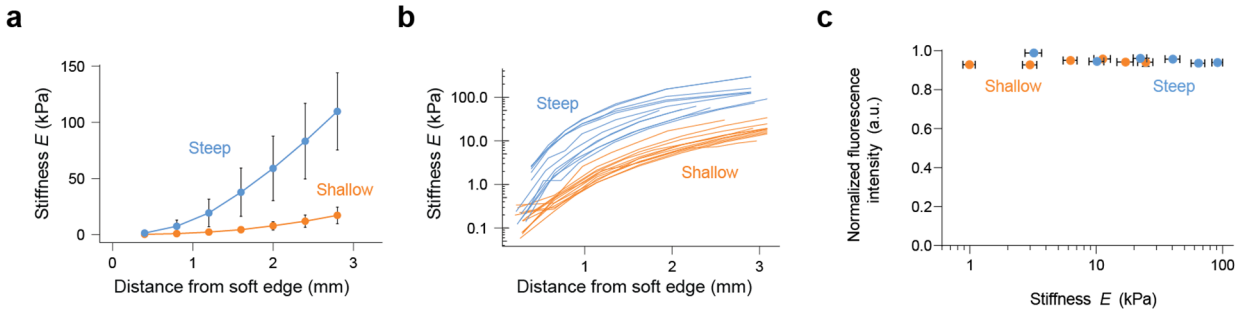

Extended Data Figure 4 | Stiffness profile and protein incorporation of shallow and steep gradient gels. a, Stiffness profile as a function of distance from soft edge for shallow (n=12, orange) and steep (n=12, blue) stiffness profiles. The stiffness profile was determined using AFM for every gel (see Methods). Data is mean ± SD. **b**, Stiffness profile for individual gels (shallow in orange, steep in blue). Note the logarithmic scale on the Stiffness axis for the sake of visualization. **c**, Normalized fluorescence intensity of histidine-tagged mCherry signal as a readout of protein incorporation as a function of stiffness for shallow and steep gradient gels.

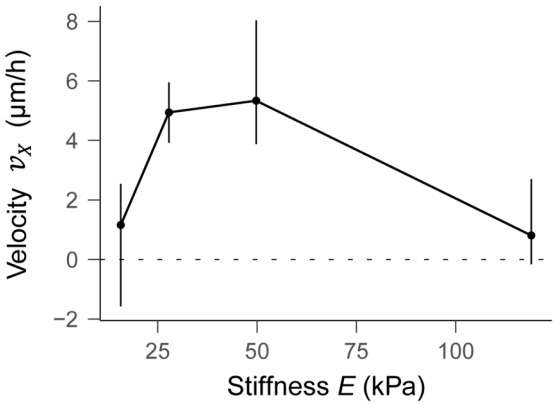

Extended Data Figure 5 | Dependence of durotactic velocity on stiffness for clusters within the 40 ± 10 kPa/mm gradient range . Data analyzed include only the positions of the gels where the gradient was 40 ± 10 kPa/mm , showing that the sharp increase of durotactic velocity with stiffness cannot be accounted for by changes in the gradient. Bin 1 ($0 < E \leq 20$ kPa): n= 28 clusters (136 displacements), E' = 36.8 kPa/mm. Bin 2 ($20 < E \leq 40$ kPa): n= 62 clusters (386 displacements), E' = 40.5 kPa/mm. Bin 3 ($40 < E \leq 80$ kPa): n= 23 clusters (102 displacements), E' = 47.8 kPa/mm. Bin 4 ($E > 80$ kPa): n= 43 clusters (313 displacements), E' = 48.8 kPa/mm. Data includes clusters of all sizes. Data is median ± 95% CI estimated by bootstrapping.

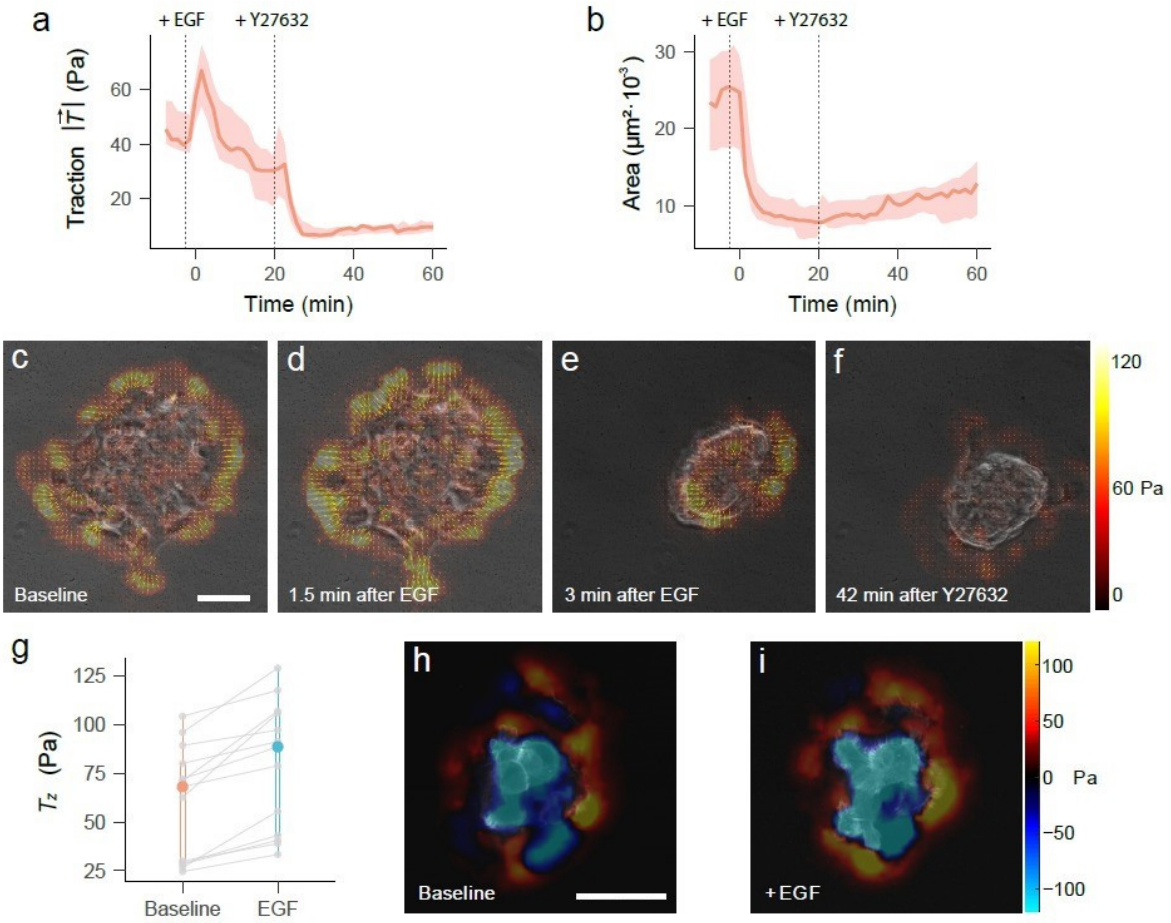

Extended Data Figure 6 | hEGF increases cell contractility and surface tension. a, Time lapse evolution of the modulus of the traction forces upon addition of 10 ng/ml of hEGF and the subsequent addition of 5µg/ml of Y27632 (indicated by vertical dashed lines). Gel stiffness is 6 kPa. **b,** Cluster area variation during the protocol described in (**a**). Data in panels **a-b** are median ± 95% CI estimated by bootstrapping (n=15 clusters). **c-f,** In-plane traction forces exerted by a representative cluster before addition of hEGF (**c**), 1.5 min after the addition of hEGF (**d**), 3 min after the addition of hEGF (**e**), and 42 min after the addition of Y27632 (**f**). **g,** The normal traction component T_z increases 2 min after adding hEGF, indicating an increase in surface tension and Laplace pressure. A paired permutation test (two-tailed) indicated a significant increase (n= 13, p-value= 0.0002441). **h-i,** T_z maps exerted by a representative cluster before (**h**) and after (**i**) the addition of hEGF.

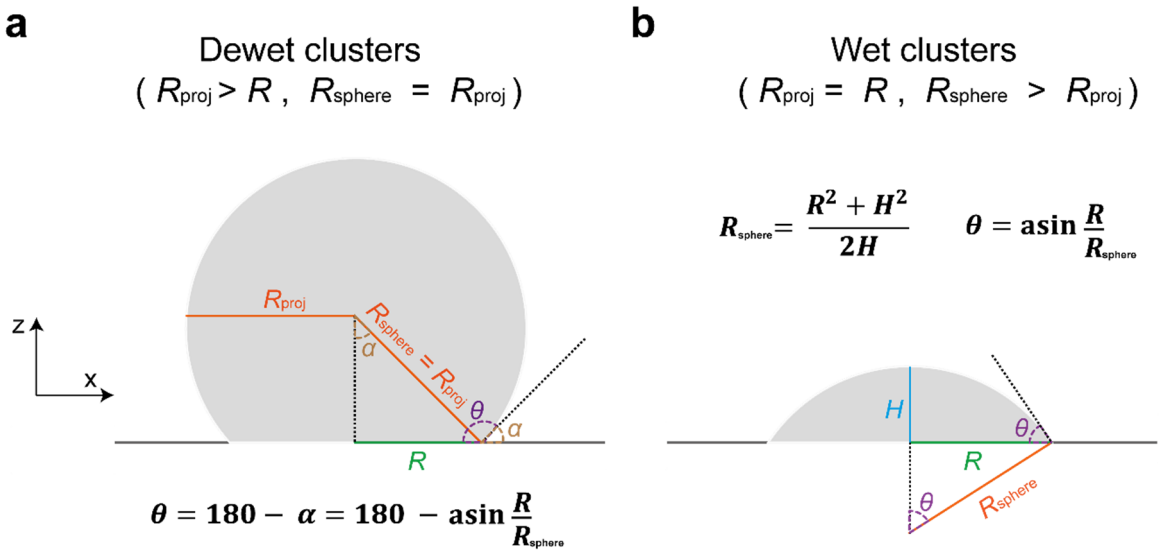

Extended Data Figure 7 | Calculation of contact angle. Measurement of contact angle θ as a function of the cluster radius (R_{sphere}), the contact radius (R) and the cluster height (H). For low wettability (**a**) and high wettability (**b**) clusters the calculation varied. All parameters were estimated from high resolution z-stacks of LifeAct-mCherry A431 clusters seeded on E-cadherin substrates.

Video legends

Supplementary video 1: Representative phase contrast video of A431 cell cluster migration on uniform stiffness gels of 0.2, 6, 24 and 200kPa coated with E-cadherin.

Supplementary video 2: z-stack movies of representative mCherry-Lifeact A431 cell clusters seeded on uniform stiffness gels of 0.2, 6, 24 and 200kPa coated with E-cadherin to illustrate cluster wetting state.

Supplementary video 3: Filopodia dynamics of representative A431 cell clusters seeded on uniform stiffness gels of 6, 24 and 200kPa coated with E-cadherin.

Supplementary video 4: Actin retrograde flow of representative A431 cell clusters seeded on uniform stiffness gels of 6, 24 and 200kPa coated with E-cadherin.

Supplementary video 5: Representative phase images of A431 cell cluster migration on a stiffness gradient coated with E-cadherin. Bottom numbers indicate stiffness in kPa.

Supplementary video 6: Migration of representative mCherry-Lifeact A341 cell clusters on a stiffness gradient (local stiffness = 10kPa) coated with E-cadherin.

Supplementary video 7: Representative phase contrast images of A431 cell cluster migration on a stiffness gradient coated with E-cadherin in controls and in presence of 0.5µM Y-27632 (ROCK inhibitor) aiming to partially inhibit cell contractility.

Supplementary video 8: Representative phase contrast images of A431 cell cluster migration on uniform stiffness gels of 0.2, 6, 24 and 200kPa coated with fibronectin in controls and in presence of 10ng/mL hEGF aiming to promote cell contractility.

Supplementary video 9: Representative phase contrast images of A431 cell cluster migration on a stiffness gradient coated with fibronectin in controls and in presence of 10ng/mL hEGF aiming to promote cell contractility.

Supplementary video 10: Phase contrast video representing an example of a sudden retraction of filopodia triggering a long durotactic hop.

References

1. Haeger, A., Wolf, K., Zegers, M. M. & Friedl, P. Collective cell migration: guidance principles and hierarchies. *Trends Cell Biol.* **25**, 556–566 (2015).

2. Majumdar, R., Sixt, M. & Parent, C. A. New paradigms in the establishment and maintenance of gradients during directed cell migration. *Curr. Opin. Cell Biol.* **30**, 33–40 (2014).

3. Lyon, J. G., Carroll, S. L., Mokarram, N. & Bellamkonda, R. V. Electrotaxis of Glioblastoma and Medulloblastoma Spheroidal Aggregates. *Sci. Rep.* **9**, 5309 (2019).

4. Lo, C. M., Wang, H. B., Dembo, M. & Wang, Y. L. Cell movement is guided by the rigidity of the substrate. *Biophys. J.* **79**, 144–152 (2000).

5. Vincent, L. G., Choi, Y. S., Alonso-Latorre, B., del Álamo, J. C. & Engler, A. J. Mesenchymal stem cell durotaxis depends on substrate stiffness gradient strength. *Biotechnol. J.* **8**, 472–484 (2013).

6. Sunyer, R. & Trepat, X. Durotaxis. *Curr. Biol.* **30**, R383–R387 (2020).

7. Shellard, A. & Mayor, R. Durotaxis: The Hard Path from In Vitro to In Vivo. *Dev. Cell* **56**, 227–239 (2021).

8. Zhu, M. *et al.* Spatial mapping of tissue properties in vivo reveals a 3D stiffness gradient in the mouse limb bud. *Proc. Natl. Acad. Sci.* **117**, 4781–4791 (2020).

9. Shellard, A. & Mayor, R. Collective durotaxis along a self-generated stiffness gradient in vivo. *Nature* **600**, 690–694 (2021).

10. Evans, N. D., Oreffo, R. O. C., Healy, E., Thurner, P. J. & Man, Y. H. Epithelial mechanobiology, skin wound healing, and the stem cell niche. *J. Mech. Behav. Biomed. Mater.* **28**, 397–409 (2013).

11. DuChez, B. J., Doyle, A. D., Dimitriadis, E. K. & Yamada, K. M. Durotaxis by Human Cancer Cells. *Biophys. J.* **116**, 670–683 (2019).

12. Sunyer, R. *et al.* Collective cell durotaxis emerges from long-range intercellular force transmission. *Science* **353**, 1157 (2016).

13. Martinez, J. S., Schlenoff, J. B. & Keller, T. C. S. Collective epithelial cell sheet adhesion and migration on polyelectrolyte multilayers with uniform and gradients of compliance. *Exp. Cell Res.* **346**, 17–29 (2016).

14. Alert, R. & Casademunt, J. Role of Substrate Stiffness in Tissue Spreading: Wetting Transition and Tissue Durotaxis. *Langmuir* **35**, 7571–7577 (2019).

15. Pi-Jaumà, I., Alert, R. & Casademunt, J. Collective durotaxis of cohesive cell clusters on a stiffness gradient. *Eur. Phys. J. E* **45**, 7 (2022).

16. Escribano, J. *et al.* A hybrid computational model for collective cell durotaxis. in *Biomech. model. mechanobiol.* **17**, 1037–1052 (2018).

17. Novikova, E. A., Raab, M., Discher, D. E. & Storm, C. Persistence-driven durotaxis: Generic, directed motility in rigidity gradients. *Phys. Rev. Lett.* **118**, 078103 (2017).

18. Isomursu, A. *et al.* Directed cell migration towards softer environments. *Nat. Mater.* 1–10 (2022).

19. Lazopoulos, K. A. & Stamenović, D. Durotaxis as an elastic stability phenomenon. *J. Biomech.* **41**, 1289–1294 (2008).

20. Yu, G., Feng, J., Man, H. & Levine, H. Phenomenological modeling of durotaxis. *Phys. Rev. E* **96**, 010402 (2017).

21. Rens, E. G. & Merks, R. M. H. Cell Shape and Durotaxis Explained from Cell-Extracellular Matrix Forces and Focal Adhesion Dynamics. *iScience* **23**, 101488 (2020).

22. Isenberg, B. C., DiMilla, P. A., Walker, M., Kim, S. & Wong, J. Y. Vascular Smooth Muscle Cell Durotaxis Depends on Substrate Stiffness Gradient Strength. *Biophys J* **97**, 1313–1322 (2009).

23. Hartman, C. D., Isenberg, B. C., Chua, S. G. & Wong, J. Y. Vascular smooth muscle cell durotaxis depends on extracellular matrix composition. *Proc. Natl. Acad. Sci.* **113**, 11190–11195 (2016).

24. Richardson, B. E. & Lehmann, R. Mechanisms guiding primordial germ cell migration: strategies from different organisms. *Nat. Rev. Mol. Cell Biol.* **11**, 37–49 (2010).

25. Cai, D. *et al.* Mechanical feedback through E-cadherin promotes direction sensing during collective cell migration. *Cell* **157**, 1146–1159 (2014).

26. Dai, W. *et al.* Tissue topography steers migrating Drosophila border cells. *Science* **370**, 987–990 (2020).

27. Grimaldi, C. *et al.* E-cadherin focuses protrusion formation at the front of migrating cells by impeding actin flow. *Nat. Commun.* **11**, 5397 (2020).

28. Dorrell, M., Aguilar, E. & Friedlander, M. Dorrell, M. I. , Aguilar, E. & Friedlander, M. Retinal vascular development is mediated by endothelial filopodia, a preexisting astrocytic template and specific R-cadherin adhesion. Invest. Ophthalmol. Vis. Sci. 43, 3500-3510. *Invest. Ophthalmol. Vis. Sci.* **43**, 3500–10 (2002).

29. Luccardini, C. *et al.* N-cadherin sustains motility and polarity of future cortical interneurons during tangential migration. *J. Neurosci. Off. J. Soc. Neurosci.* **33**, 18149–18160 (2013).

30. Padmanaban, V. *et al.* E-cadherin is required for metastasis in multiple models of breast cancer. *Nature* **573**, 439–444 (2019).

31. Pérez-González, C. *et al.* Active wetting of epithelial tissues. *Nat. Phys.* **15**, 79–88 (2019).

32. Douezan, S. *et al.* Spreading dynamics and wetting transition of cellular aggregates. *Proc. Natl. Acad. Sci. U. S. A.* **108**, 7315–7320 (2011).

33. Douezan, S., Dumond, J. & Brochard-Wyart, F. Wetting transitions of cellular aggregates induced by substrate rigidity. *Soft Matter* **8**, 4578–4583 (2012).

34. Gonzalez-Rodriguez David, Guevorkian Karine, Douezan Stéphane, & Brochard-Wyart Françoise. Soft Matter Models of Developing Tissues and Tumors. *Science* **338**, 910–917 (2012).

35. Beaune, G. *et al.* How cells flow in the spreading of cellular aggregates. *Proc. Natl. Acad. Sci.* **111**, 8055–8060 (2014).

36. Wallmeyer, B., Trinschek, S., Yigit, S., Thiele, U. & Betz, T. Collective Cell Migration in Embryogenesis Follows the Laws of Wetting. *Biophys. J.* **114**, 213–222 (2018).

37. Beaune, G. *et al.* Spontaneous migration of cellular aggregates from giant keratocytes to running spheroids. *Proc. Natl. Acad. Sci. U. S. A.* **115**, 12926–12931 (2018).

38. Alert, R. & Trepat, X. Physical Models of Collective Cell Migration. *Annu. Rev. Condens. Matter Phys.* **11**, 77–101 (2020).

39. Riveline, D. *et al.* Focal contacts as mechanosensors: externally applied local mechanical force induces growth of focal contacts by an mDia1-dependent and ROCK-independent mechanism. *J. Cell Biol.* **153**, 1175–1186 (2001).

40. Ghibaudo, M. *et al.* Traction forces and rigidity sensing regulate cell functions. *Soft Matter* **4**, 1836–1843 (2008).

41. Elosegui-Artola, A. *et al.* Mechanical regulation of a molecular clutch defines force transmission and transduction in response to matrix rigidity. *Nat. Cell Biol.* **18**, 540–548 (2016).

42. Barry, A. K. *et al.* α-Catenin cytomechanics – role in cadherin-dependent adhesion and mechanotransduction. *J. Cell Sci.* **127**, 1779–1791 (2014).

43. Sunyer, R., Jin, A. J., Nossal, R. & Sackett, D. L. Fabrication of Hydrogels with Steep Stiffness Gradients for Studying Cell Mechanical Response. *PLoS ONE* **7**, e46107 (2012).

44. Blanch-Mercader, C. *et al.* Effective viscosity and dynamics of spreading epithelia: a solvable model. *Soft Matter* **13**, 1235–1243 (2017).

45. Walcott, S. & Sun, S. X. A mechanical model of actin stress fiber formation and substrate elasticity sensing in adherent cells. *Proc. Natl. Acad. Sci.* **107**, 7757–7762 (2010).

46. Saez, A. *et al.* Traction forces exerted by epithelial cell sheets. *J. Phys. Condens. Matter* **22**, 194119 (2010).

47. Marcq, P., Yoshinaga, N. & Prost, J. Rigidity sensing explained by active matter theory. *Biophys. J.* **101**, L33-35 (2011).

48. Trichet, L. *et al.* Evidence of a large-scale mechanosensing mechanism for cellular adaptation to substrate stiffness. *Proc. Natl. Acad. Sci.* **109**, 6933–6938 (2012).

49. Sens, P. Rigidity sensing by stochastic sliding friction. *Europhys. Lett.* **104**, 38003 (2013).

50. Gupta, M. *et al.* Adaptive rheology and ordering of cell cytoskeleton govern matrix rigidity sensing. *Nat. Commun.* **6**, 7525 (2015).

51. Guevorkian, K., Colbert, M.-J., Durth, M., Dufour, S. & Brochard-Wyart, F. Aspiration of biological viscoelastic drops. *Phys. Rev. Lett.* **104**, 218101 (2010).

52. Guevorkian, K., Gonzalez-Rodriguez, D., Carlier, C., Dufour, S. & Brochard-Wyart, F. Mechanosensitive shivering of model tissues under controlled aspiration. *Proc. Natl. Acad. Sci.* **108**, 13387–13392 (2011).

53. Manning, M. L., Foty, R. A., Steinberg, M. S. & Schoetz, E.-M. Coaction of intercellular adhesion and cortical tension specifies tissue surface tension. *Proc. Natl. Acad. Sci.* **107**, 12517–12522 (2010).

54. Chan, G. K., McGrath, J. A. & Parsons, M. Spatial activation of ezrin by epidermal growth factor receptor and focal adhesion kinase co-ordinates epithelial cell migration. *Open Biol.* **11**, 210166 (2021).

55. Iwabu, A., Smith, K., Allen, F. D., Lauffenburger, D. A. & Wells, A. Epidermal growth factor induces fibroblast contractility and motility via a protein kinase C delta-dependent pathway. *J. Biol. Chem.* **279**, 14551–14560 (2004).

56. Czirók, A., Schlett, K., Madarász, E. & Vicsek, T. Exponential Distribution of Locomotion Activity in Cell Cultures. *Phys. Rev. Lett.* **81**, 3038–3041 (1998).

57. Wu, P.-H., Giri, A., Sun, S. X. & Wirtz, D. Three-dimensional cell migration does not follow a random walk. *Proc. Natl. Acad. Sci.* **111**, 3949–3954 (2014).

58. González-Valverde, I. & García-Aznar, J. M. Mechanical modeling of collective cell migration: An agent-based and continuum material approach. *Comput. Methods Appl. Mech. Eng.* **337**, 246–262 (2018).

59. Garcia-Gonzalez, D. & Muñoz-Barrutia, A. Computational insights into the influence of substrate stiffness on collective cell migration. *Extreme Mech. Lett.* **40**, 100928 (2020).

60. Deng, Y., Levine, H., Mao, X. & Sander, L. M. Collective Motility, Mechanical Waves, and Durotaxis in Cell Clusters. *ArXiv:2007.10488* [physics.bio-ph] (2020).

61. Yousafzai, M. S. *et al.* Active Regulation of Pressure and Volume Defines an Energetic Constraint on the Size of Cell Aggregates. *Phys. Rev. Lett.* **128**, 048103 (2022).

62. Yousafzai, M. S. *et al.* Tissue pressure and cell traction compensate to drive robust aggregate spreading. *bioRxiv:2020.08.29.273334* (2020).

63. Style, R. W. *et al.* Patterning droplets with durotaxis. *Proc. Natl. Acad. Sci.* **110**, 12541–12544 (2013).

64. Style, R. W., Jagota, A., Hui, C.-Y. & Dufresne, E. R. Elastocapillarity: Surface Tension and the Mechanics of Soft Solids. *Annu. Rev. Condens. Matter Phys.* **8**, 99–118 (2017).

65. Babb, S. G. & Marrs, J. A. E-cadherin regulates cell movements and tissue formation in early zebrafish embryos. *Dev. Dyn.* **230**, 263–277 (2004).

66. Shimizu, T. *et al.* E-cadherin is required for gastrulation cell movements in zebrafish. *Mech. Dev.* **122**, 747–763 (2005).

67. Shamir, E. R. *et al.* Twist1-induced dissemination preserves epithelial identity and requires E-cadherin. *J. Cell Biol.* **204**, 839–856 (2014).

68. Giannone, G., Mège, R.-M. & Thoumine, O. Multi-level molecular clutches in motile cell processes. *Trends Cell Biol.* **19**, 475–486 (2009).

69. Nguyen, T. *et al.* Enhanced cell–cell contact stability and decreased N-cadherin-mediated migration upon fibroblast growth factor receptor-N-cadherin cross talk. *Oncogene* **38**, 6283–6300 (2019).

70. Rakshit, S., Zhang, Y., Manibog, K., Shafraz, O. & Sivasankar, S. Ideal, catch, and slip bonds in cadherin adhesion. *Proc. Natl. Acad. Sci.* **109**, 18815–18820 (2012).

71. Changede, R. & Sheetz, M. Integrin and cadherin clusters: A robust way to organize adhesions for cell mechanics. *BioEssays* **39**, e201600123 (2017).

72. Bays, J. L. *et al.* Vinculin phosphorylation differentially regulates mechanotransduction at cell–cell and cell–matrix adhesions. *J. Cell Biol.* **205**, 251–263 (2014).

73. Sehgal, P. *et al.* Epidermal growth factor receptor and integrins control force-dependent vinculin recruitment to E-Cadherin junctions. *J Cell Sci* **15**, 131 (2018).

74. Tewari, S. *et al.* Statistics of shear-induced rearrangements in a two-dimensional model foam. *Phys. Rev. E* **60**, 4385–4396 (1999).

75. Ben-Zion, Y. & Rice, J. R. Slip patterns and earthquake populations along different classes of faults in elastic solids. *J. Geophys. Res. Solid Earth* **100**, 12959–12983 (1995).

76. Sethna, J. P., Dahmen, K. A. & Myers, C. R. Crackling noise. *Nature* **410**, 242–250 (2001).

77. Barriga, E. H., Franze, K., Charras, G. & Mayor, R. Tissue stiffening coordinates morphogenesis by triggering collective cell migration in vivo. *Nature* **554**, 523–527 (2018).

78. Tiscornia, G., Singer, O. & Verma, I. M. Production and purification of lentiviral vectors. *Nat. Protoc.* **1**, 241–245 (2006).

79. Chevalier, S. *et al.* Creating Biomimetic Surfaces through Covalent and Oriented Binding of Proteins. *Langmuir* **26**, 14707–14715 (2010).

80. Gräslund, S. *et al.* Protein production and purification. *Nat. Methods* **5**, 135–146 (2008).

81. Trepat, X. *et al.* Physical forces during collective cell migration. *Nat. Phys.* **5**, 426–430 (2009).

82. Rico, F. *et al.* Probing mechanical properties of living cells by atomic force microscopy with blunted pyramidal cantilever tips. *Phys. Rev. E* **72**, 021914 (2005).

83. Alcaraz, J. *et al.* Microrheology of Human Lung Epithelial Cells Measured by Atomic Force Microscopy. *Biophys. J.* **84**, 2071–2079 (2003).

Supplementary Note
Stiffness-dependent active wetting enables optimal collective cell durotaxis

Macià-Esteve Pallarès, Irina Pi-Jaumà, Isabela Corina Fortunato, Valeria Grazú, Manuel Gómez-González, Pere Roca-Cusachs, Jesús M de la Fuente, Ricard Alert, Raimon Sunyer, Jaume Casademunt, Xavier Trepat

Here, we present a theoretical framework to explain collective durotaxis of cell clusters in terms of a continuum model of the tissue. To this end, we describe a cell cluster as an active fluid droplet that partially wets the substrate. Extending a previous 2D model of tissue wetting, we first develop a theory of 3D active wetting for tissues on a uniform substrate. In this theory, the contact line dynamics results from the balance between the in-plane forces acting at the basal monolayer and the out-of-plane surface tension of the cell cluster, defining a dynamic contact angle. We then apply this theory to predict cluster durotaxis on a substrate stiffness gradient, explaining the generic non-monotonic dependence of the durotactic velocity with substrate stiffness observed in our experiments. Our analysis shows that the existence of an optimal stiffness for collective durotaxis is connected to the wetting properties of the droplet, which depend on stiffness. In particular we show that the maximum of durotactic velocity occurs near the point where the contact angle crosses over 90 degrees. We then study how the durotactic velocity varies with the mechanical parameters of the tissue, which allows us to explain the dependence of durotaxis on tissue size and cellular contractility observed in our experiments.

1 Theory of 3D active wetting

We describe a cell cluster on a substrate as an active liquid droplet that partially wets a solid surface with a contact angle θ (Fig. 3a). The interface between the cell cluster and the surrounding passive fluid has a surface tension γ, which results from a combination of passive cell-cell adhesion and active cortical tension [1–5]. Averaging out tissue shape fluctuations, we describe the cell cluster as a spherical cap of radius R. We assume that the bulk of the cell cluster is passive, and that the dynamics of the droplet is determined by the interplay of its surface tension and the in-plane forces at the basal cell monolayer. Following previous work [6], we model the basal cell monolayer as a 2D active polar fluid. We then extend this model to 3D by proposing a generalized Young-Dupré force balance that includes the out-of-plane contribution of surface tension. This new ingredient modifies the contact line dynamics and defines the droplet's dynamic contact angle. Then, taking active cellular forces that depend on substrate stiffness [7–12], we predict how this environmental property affects the droplet's contact angle and spreading dynamics. Finally, we use our theory to show how these stiffness-dependent wetting properties give rise to collective durotaxis of cell clusters on stiffness gradients.

1.1 2D model of the basal cell monolayer

Following Refs. [6, 13–15], we model the basal cell monolayer as a 2D active polar fluid described by two fields, cell polarity $\boldsymbol{p}(\boldsymbol{r},t)$ and velocity $\boldsymbol{v}(\boldsymbol{r},t)$. We assume that the polarity field is independent of the flow field, since the timescale of cell repolarization through contact inhibition of locomotion ($\tau_{\mathrm{CIL}} \sim 10$ min [16, 17]) is much smaller than the typical shear rate of flows in the monolayer ($\tau \sim 100$ min [18, 19]). Thus, the polarity field follows a purely relaxational dynamics, $\partial_t p_\alpha \propto -\delta F/\delta p_\alpha$. The tendency of cells to align with

their neighbors is encoded in the effective free energy

$$F = \int \left[\frac{a}{2} p_\alpha p_\alpha + \frac{K}{2} (\partial_\alpha p_\beta)(\partial_\alpha p_\beta) \right] \mathrm{d}^2 \boldsymbol{r}, \tag{S1}$$

being K the Frank constant that defines the energetic cost of the polarity gradients [20], and $a > 0$ a restoring coefficient that favors the unpolarized state $p = 0$ in the bulk. We further assume a quasistatic evolution of the polarity $\partial_t p_\alpha = 0$, hence

$$L_c^2 \nabla^2 p_\alpha = p_\alpha, \tag{S2}$$

where $L_c \equiv \sqrt{K/a}$ is the nematic length that defines the width of a boundary layer in which cells are polarized at the periphery of the monolayer. Since cells at the edge are polarized toward free space, we impose the boundary condition $p_\alpha = n_\alpha$, where n_α is the outward normal vector. Solving Eq. (S2) with this boundary condition, the modulus of the polarity decays from one at the edge to zero in the bulk over the characteristic length L_c.

We describe tissue flow based on the force balance equation

$$\partial_\beta \sigma_{\alpha\beta} + f_\alpha = 0, \tag{S3}$$

where $\sigma_{\alpha\beta}$ is the stress tensor, and f_α is the external force density originated at the tissue-substrate interface. Note that the experimentally measured monolayer tension and traction are $\sigma_{\alpha\beta} h$ and $T_\alpha \equiv -f_\alpha h$, respectively, being h the height of the monolayer. In Eq. (S3) we have neglected inertia, consistently with the small values of Reynolds number for tissue flows. We have also neglected pressure gradients by assuming that the 2D fluid is highly compressible as in-plane compression and expansion are accommodated by local changes in the monolayer thickness, without significant changes in pressure [21].

As tissue spreading takes place over very long time scales, we neglect the short-time elastic response of the tissue and assume a purely viscous response [21]. Hence, we take the constitutive equation for the stress tensor of a compressible active viscous polar fluid [22–26]. This includes two main contributions: active contractile stresses originated in cell-cell forces and quantified by the contractility parameter $\zeta < 0$, and viscous stresses that result from cell-cell adhesion forces and are weighted by an effective viscosity η. Similarly, the cell-substrate force density f_α has two main contributions: an active traction force that is proportional to polarity $\boldsymbol{p}$ and with a maximum value ζ_i, and a friction force due to cell-substrate adhesion, proportional to the tissue velocity $\boldsymbol{v}$ and with a coefficient ξ [6, 27]. Altogether,

$$\sigma_{\alpha\beta} = \eta(\partial_\alpha v_\beta + \partial_\beta v_\alpha) - \zeta p_\alpha p_\beta, \tag{S4}$$

$$f_\alpha = -\xi v_\alpha + \zeta_i p_\alpha. \tag{S5}$$

To complete the model we need to specify the boundary conditions for the stress. This is the point where the effect of the 3D shape of cell cluster will be incorporated, so we defer this discussion to Section 1.3.

1.2 The 2D active wetting transition for cell monolayers

The 2D model of tissue spreading presented above predicts an active wetting transition in cell monolayers, which was verified in experiments [6]. This transition has no analogue in the classical theory of wetting; it results from the competition between active traction that favors tissue spreading and contractile stresses that favor retraction. The transition is controlled by a characteristic length of active polar fluids, defined as the ratio of contractile nematic stresses to active polar forces: $L_p \equiv |\zeta|/\zeta_i$. The active wetting transition takes place at a critical value L_p^*: the tissue spreads for $L_p < L_p^*$ (wetting), and it retracts for $L_p > L_p^*$ (dewetting).

The physical properties of this active wetting transition depend on whether dissipation is dominated by the internal tissue viscosity η or by the external friction ξ. The comparison of these two effects defines the so-called screening length $\lambda \equiv \sqrt{\eta/\xi}$, which indicates an effective range of hydrodynamic interactions. The limit $\lambda \to \infty$ is known as the 'wet' limit, for which hydrodynamic interactions are long-ranged; the limit $\lambda \to 0$ is known as the 'dry' limit, for which hydrodynamic interactions are screened out by friction.

The study of 2D active wetting in Ref. [6] considered circular monolayers in the 'wet' limit. In that case, $L_p^* \sim R$, with R being the monolayer radius. Therefore, the wetting transition occurs at a critical radius R^*: larger monolayers $R > R^*$ spread, and smaller monolayers $R < R^*$ retract. The existence of a critical radius illustrates the non-local character of active wetting in the 'wet' limit. In contrast to classic wetting theory, the advance or recession of the tissue front is not determined by local forces at the interface, but by the system as a whole. More recent works have considered the 'dry' limit, when friction forces are dominant over viscosity [13–15]. In this case, $L_p^* \sim \lambda$ [15], so there is no critical size for the wetting-dewetting transition. In this limit, the advance or recession of the front is determined by the local forces at the interface, and hence the wetting transition is size-independent.

Here, we will address the generic case and keep both friction and viscosity. For simplicity, we will solve the active wetting problem considering only one dimension ($\hat{\boldsymbol{x}}$), along which the cell monolayer spreads or retracts (Fig. 3a). This corresponds to assuming translational invariance along the perpendicular direction. The predictions for the active wetting transition in this one-dimensional geometry differ only in geometrical factors from those for circular cell monolayers [6, 13–15]. In addition, the one-dimensional geometry is particularly suited when tissue migration is biased by external gradients, such as in the experiments on collective durotaxis with rectangular cell monolayers [28]. It also yields a good approximation for the migration of circular monolayers as tissue flows occur mainly in the direction of the imposed gradient [15]. In the one-dimensional geometry, Eqs. (S3) to (S5) combine into

$$2\eta\partial_x^2 v = 2\zeta p \partial_x p + \xi v - \zeta_i p, \tag{S6}$$

where

$$p(x) = \frac{\sinh\left((x-X)/L_c\right)}{\sinh\left(R/L_c\right)} \tag{S7}$$

is the solution of Eq. (S2), with R being the monolayer half-width (radius), and X being the center-of-mass position. Given x_+ and x_- the positions of the two edges of the monolayer, we have $X \equiv (x_+ + x_-)/2$ and $R \equiv (x_+ - x_-)/2$. With the solution of the velocity profile $v(x)$ at a given time, the velocity of the center-of-mass v_X and the spreading velocity v_S are given by

$$v_X \equiv \dot{X} = \frac{v(x_+) + v(x_-)}{2}, \quad v_S \equiv \dot{R} = \frac{v(x_+) - v(x_-)}{2}. \tag{S8}$$

In the absence of an external gradient, we have $v_X = 0$. However, v_S may be positive when the monolayer is spreading (wetting), or negative when it is retracting (dewetting). The 2D wetting transition is thus defined by $v_S = 0$.

For reference, we quote the results for the spreading velocity v_S in both the wet and the dry limits. Assuming $L_c \ll R, \lambda$, and with stress-free boundary conditions at the monolayer edge, we have [15]

$$v_S^{\mathrm{wet}} \approx \frac{L_c \zeta_i}{2\eta}\left(R - \frac{L_p}{2}\right), \tag{S9}$$

$$v_S^{\mathrm{dry}} \approx \frac{L_c \zeta_i}{2\eta}\left(\sqrt{2}\lambda - \frac{L_p}{2}\right). \tag{S10}$$

1.3 Generalized Young-Dupré equilibrium for 3D cell clusters

Here, we extend the theory of active wetting to 3D cell clusters. To this end, we add the contribution of the out-of-plane surface tension γ of the cell cluster to the 2D model of the basal cell monolayer presented above (Fig. 3a). As discussed, for stress-free boundary conditions, a cell monolayer either spreads or retracts indefinitely as a result of the competition between active traction and contractility. However, for 3D droplets, the surface tension γ introduces an additional force that can either favor spreading or retraction depending on the contact angle θ. For $\theta > 90°$, surface tension favors spreading (Fig. 3a left), whereas for $\theta < 90°$, surface tension favors retraction (Fig. 3a right). For sufficiently large surface tension, and depending on parameter values, all three active forces may balance and the droplet may reach a partial wetting state, namely a stable equilibrium with a finite contact angle θ (Figs. S1 and S2).

In classical wetting theory, the equilibrium contact angle is determined by the Young-Dupré condition, which establishes the balance of the three surface tensions at the contact line. For cell aggregates, a similar

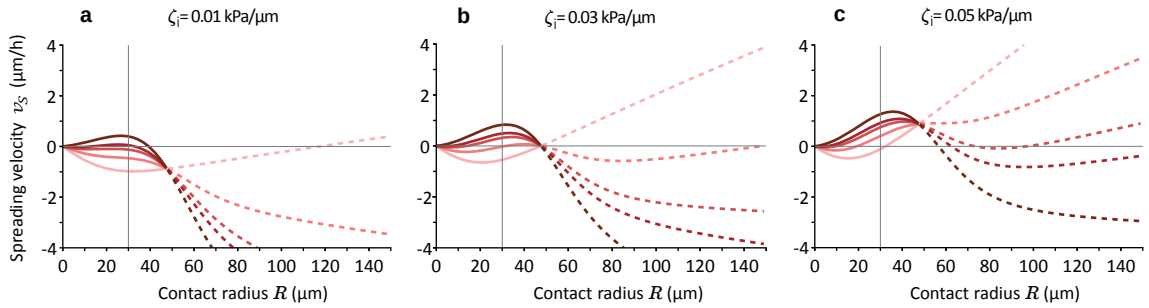

Figure S1. Roots of the spreading velocity define the partial wetting state for sufficiently large surface tension γ. Spreading velocity of a cluster on top of a uniform-stiffness substrate as a function of the contact radius R, for different values of active traction (**a-c**) and surface tension $\gamma = 0, 1.5, 2.5, 3, 4$ mN/m (from lighter to darker red). The other parameter values are those from Table SI, with a constant friction $\xi = 0.22$ kPa s/µm^2. The volume is kept constant to $V = 2/3\pi R^{*3}$, being $R^* = 47.6$ µm the radius at the 2D wetting transition for $\zeta_i = 0.03$ kPa/µm (**b**). We switch from solid to dashed lines when the cluster has a contact angle of 90° ($R = R_{\text{sphere}} = H$), and so the continuous lines correspond to angles $\theta > 90°$ ($R < R^*$) and the dashed lines to angles $\theta < 90°$ ($R > R^*$). The vertical line at each panel is drawn at $R = 30$ µm, which is the initial size (R_0) chosen for the dynamics in Fig. S2. From this point, we can predict whether a cluster will converge to the stable fixed point ($v_S(R_0) > 0$ with roots), or will completely dewet ($v_S(R_0) < 0$) or wet the substrate ($v_S(R_0) > 0$ without roots).

energetic approach was proposed to define the wetting conditions in terms of the cell-cell and cell-substrate adhesion energies [29–32]. This approach, however, does not explicitly account for active cellular forces, which have a key role in tissue wetting [6]. Following Ref. [6], here we assume that the surface tension of the interface between the surrounding passive fluid and the substrate is negligible in front of the active forces. Consistently, we propose a generalized Young-Dupré condition that captures a balance of three active forces: active traction and contractility, which are distributed in the polarized layer of the basal cell monolayer, and the cluster's surface tension, which enters as a local force at the contact line. Hence, we include the horizontal component of surface tension into the monolayer force balance Eq. (S6) as a stress boundary condition:

$$n_\alpha (h\sigma_{\alpha\beta}) n_\beta = -\gamma \cos\theta, \tag{S11}$$

where n_β is the unit normal vector at the monolayer edge, and $h\sigma_{\alpha\beta}$ is the monolayer tension, with h the monolayer height. In turn, the vertical component of the surface tension is balanced by the Young-Laplace pressure $P = 2\gamma/R_{\text{sphere}}$, which the cell cluster exerts on the substrate. This relationship allows us to infer γ from measurements of vertical traction forces (Fig. 1g-j), which provide a direct measurement of P (see table 2 in Methods).

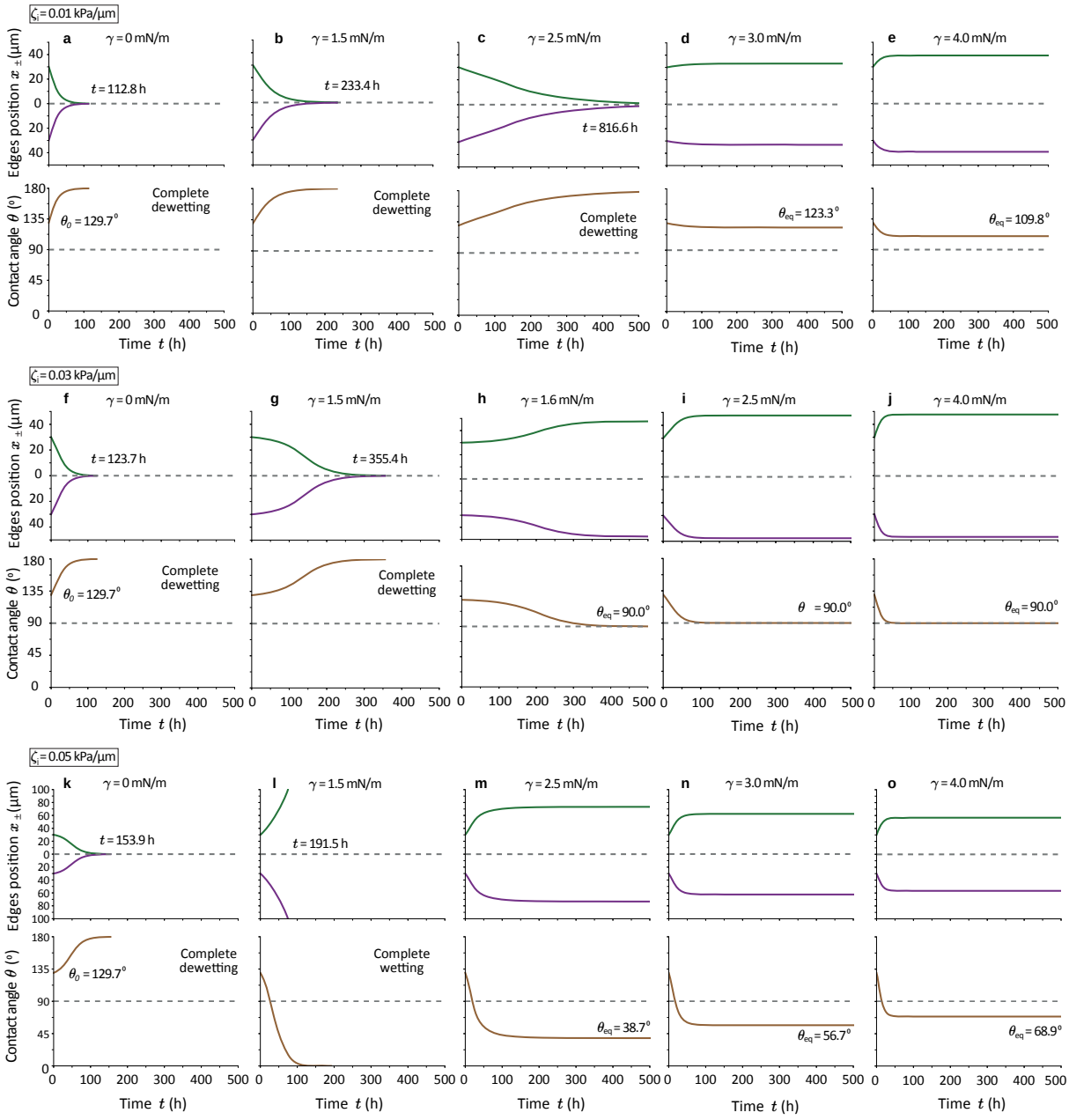

Figure S2. Cell clusters reach an equilibrium state of partial wetting for sufficiently large surface tension γ. Evolution of the position of the edges of the basal cell monolayer (green for right x_+, and purple for left x_-) and the contact angle of a cluster on top of a uniform-stiffness substrate. We show the evolution for three different values of the active traction (**a-e**, **f-j** and **k-o**), and for different values of surface tension, increasing from left to right. In all cases, the initial contact radius is $R_0 = 30$ μm and the height $H_0 = 63.9$ μm, giving a volume (which is kept constant throughout the evolution) of $V = 2/3\pi R^{*3}$, being $R^* = 47.6$ μm the radius at the 2D wetting transition for $\zeta_i = 0.03$ kPa/μm. The parameters are those from Table SI, with $\xi = 0.22$ kPa s/μm^2, a simulation time $T = 500$h and a time step $\Delta t = 6$ min. **a-e**, For $\gamma = 0$ mN/m (**a**), the cluster fully dewets the substrate (defined when it reaches $R \leq 0.1$ μm) after 112.8h. Increasing surface tension to $\gamma = 1.5, 2.5, 3, 4$ mN/m (**b**,**c**,**d**,**e**), the cluster reaches the equilibrium contact angle only if γ is large enough, with $\theta_{\rm eq} = 123.3, 109.8°$ (**d** and **e**). **f-j**, For $\gamma = 0$ mN/m (**f**), the cluster fully dewets the substrate after 123.7h. With $\gamma = 1.5, 1.6, 2.5, 4$ mN/m (**g**,**h**,**i**,**j**), the cluster reaches the equilibrium contact angle of $\theta_{\rm eq} = 90°$ only if γ is large enough. **k-o**, For $\gamma = 0$ mN/m (**k**), the cluster fully wets the substrate (defined when it reaches $H \leq 0.1$ μm) after 153.9h. With $\gamma = 1.5, 2.5, 3, 4$ mN/m (**l**,**m**,**n**,**o**), the cluster reaches the equilibrium contact angle only if γ is large enough, with $\theta_{\rm eq} = 38.7, 56.7, 68.9°$. The larger γ, the closer is $\theta_{\rm eq}$ to 90°.

	Description	Typical value
h	Monolayer height	5 µm [6, 33]
L_c	Nematic length	15 µm [6, 18]
η	Monolayer viscosity	20 MPa s [6, 18]
ζ	Monolayer contractility	-2 kPa [6]
λ	Hydrodynamic screening length	4.2×10^2 µm
E_0	Substrate's softest stiffness	0.5 kPa (Fig. 2a)
E'	Stiffness gradient	33 kPa/mm (Fig. 2a)
E^*	Characteristic stiffness of force saturation	140 kPa [31]
ζ_i^∞	Traction saturation value	0.3 kPa/µm [6, 18]
ξ^∞	Friction saturation value	0.5 kPa s/µm^2 [34]
ξ_0	Friction at $E \to 0$	2.2×10^{-1} kPa s/µm^2
P_{0x}	Pressure at E_0	4.2 Pa
s_P	Pressure sensitivity to stiffness	1.8×10^{-2}

Table SI. Symbols and typical values of model parameters, of the same order of magnitude as in the references.

2 Collective durotaxis of 3D cell clusters

2.1 Stiffness-dependent forces

In this section, we study collective durotaxis of cell clusters by imposing a gradient of substrate stiffness. Following previous work [14, 15], we assume that the parameters that encode tissue-substrate interactions depend on the local substrate stiffness. This functional dependence must be determined independently and is an input into our hydrodynamic model. From Refs. [7–12], we assume that both friction and traction parameters saturate to maximal values at high stiffness, and hence we take

$$\zeta_i(E) = \zeta_i^\infty \frac{E}{E + E^*}, \quad \xi(E) = \xi^\infty \frac{E}{E + E^*} + \xi_0, \tag{S12}$$

where ζ_i^∞ and ξ^∞ are saturation values, and E^* is a characteristic stiffness of force saturation. Finally, ξ_0 is the friction coefficient at vanishing substrate stiffness, which we add to avoid the strict 'wet' limit $\lambda \to \infty$ ($\xi \to 0$). This limit is ill-defined in presence of a traction gradient, because global force balance cannot be satisfied in the absence of friction[1].

In our experimental measurements, not only radial in-plane tractions (Fig. 1g-i) but also out-of-plane tractions (Fig. 1g,h,j) increase with substrate stiffness. We model this mechanosensitive response of the tissue surface tension by making the pressure $P(E)$ increase with substrate stiffness. For simplicity, and because there is no experimental evidence, to our knowledge, of saturation of out-of-plane tractions with stiffness, we assume a linear dependence

$$P(E) = P_0 + s_P E. \tag{S13}$$

We call s_P the pressure sensitivity to stiffness. Via the Young-Laplace relation, the pressure dependence on stiffness corresponds to a stiffness-dependent surface tension

$$\gamma(E) = \frac{R_{\text{sphere}}}{2} P(E) = \gamma_0 + \ell_\gamma E, \tag{S14}$$

where $\gamma_0 = P_0 R_{\text{sphere}}/2$ is the bare surface tension, and we call $\ell_\gamma = s_P R_{\text{sphere}}/2$ the stiffness response length. Note that when the radius of the spherical cap R_{sphere} varies, as in dynamical evolutions with constant droplet volume V, γ_0 and ℓ_γ also vary accordingly.

[1] To see this, consider the total traction, i.e., the cell-substrate force density given by Eq. (S5): $\boldsymbol{f} = -\xi \boldsymbol{v} + \zeta_i \boldsymbol{p}$. In the absence of friction, we have $\boldsymbol{f} = \zeta_i \boldsymbol{p}$, whose integral over the tissue, $\int \boldsymbol{f}\, \mathrm{d}^2\boldsymbol{r}$, does not vanish if the traction is different on the stiff and the soft edges.

2.2 Durotaxis of 2D cell monolayers

Before analyzing the full 3D problem, we discuss the durotactic migration of a 2D cell monolayer. To this end, we take a linear stiffness profile

$$E(x) = E_0 + E'x, \tag{S15}$$

being E_0 and E' the stiffness offset and gradient, respectively. Introducing the stiffness profile in Eqs. (S13) and (S14), we obtain the pressure and surface tension profiles

$$P(x) = P_{0x} + P'x = (P_0 + s_P E_0) + s_P E'x \tag{S16}$$

$$\gamma(x) = \gamma_{0x} + \gamma'x = (\gamma_0 + \ell_\gamma E_0) + \ell_\gamma E'x. \tag{S17}$$

Furthermore, to reduce the number of parameters and gain physical insight, we momentarily replace the saturating traction and friction coefficients given in Eq. (S12) by non-saturating linear functions of substrate stiffness E, or equivalently, of the position x along the stiffness gradient:

$$\zeta_i(x) = \zeta_i^0 + \zeta_i'x, \quad \xi(x) = \xi_0 + \xi'x, \tag{S18}$$

where ζ_i' and ξ' are the traction and friction gradients, respectively. We further simplify the problem by taking a uniform friction ($\xi' = 0$). In this case, Eq. (S6) can be solved analytically to obtain the velocity field, which was done Appendix B of Ref. [15]. In the dry and wet limits, and assuming $L_c \ll R, \lambda$, the center-of-mass velocity or durotactic velocity v_X does not depend on the boundary conditions of the stress, and we obtain

$$v_X^{\text{dry}} \approx \frac{L_c\lambda}{2\eta} R\zeta_i' = \frac{L_c\lambda}{4\eta}(\zeta_i^+ - \zeta_i^-), \tag{S19}$$

$$v_X^{\text{wet}} \approx \frac{L_c\lambda^2}{2\eta}\zeta_i' = \frac{L_c\lambda^2}{4\eta}\frac{\zeta_i^+ - \zeta_i^-}{R}, \tag{S20}$$

where $\zeta_i^\pm$ are the local values of the active traction at the respective edges. In both cases, the spreading velocity v_S has the same expression as in uniform-stiffness situations (Eqs. (S9) and (S10)) albeit replacing ζ_i by $\zeta_i(X)$, i.e. the active traction at the center-of-mass X.

In the dry limit, the spreading dynamics is local in the sense that the two edges move independently from the other, driven only by local forces at the edges. Thus, the durotactic velocity is directly proportional to the traction difference across the tissue, and hence to the monolayer size (Eq. (S19)). In contrast, in the wet limit the two edges are hydrodynamically coupled, and the durotactic velocity depends directly on the traction difference and inversely on the monolayer size R (Eq. (S20)). These two dependencies cancel each other, and the durotactic velocity is independent of the monolayer size in this case (Eq. (S20)).

In this simplest situation with a uniform traction gradient ζ_i' and uniform friction ($\xi' = 0$), the durotactic velocity of a cell monolayer is independent of the traction offset ζ_i^0, and hence of the local substrate stiffness [15]. This behavior cannot explain our experimental measurements, which show a non-monotonic dependence of durotactic velocity with substrate stiffness (Fig. 2e,f).

2.3 Non-monotonic durotaxis of 3D cell clusters

In this section we explain the non-monotonic dependence of durotactic velocity with substrate stiffness measured in our experiments (Fig. 2e,f). We show that this non-monotonic behavior arises from a combination of different effects: a) Both the increase of friction and the saturation of traction with stiffness produce a decrease of durotactic velocity at high stiffness, and b) the variation of the contact angle, which is controlled by the out-of-plane surface tension, produces an increase of durotactic velocity at low stiffness. The competition of these opposite trends yields a maximal durotactic velocity at an intermediate stiffness, for which durotaxis is optimal. We also show that this maximum occurs near the point where the contact angle crosses over 90°, which separates the conditions of low and high wettability. We call this region the neutral wetting regime.

To show this, we use the model to predict the evolution of the velocity and the shape of a cluster as it migrates toward stiffer regions, numerically integrating the dynamics of a cluster with constant volume (see Methods). A representative result is shown in Fig. 3b,c, which we discuss in the Main Text.

We remark that in our present model the wetting properties are defined globally for the cluster as a whole, and so we cannot contemplate contact angle differences at both edges due to different stiffness. However, the dominant asymmetry that drives durotaxis is the difference between tractions at both edges [15], so a contact angle asymmetry would enter only as a higher order correction. We will study this contribution in future work, including shape variations and deformability of the substrate.

2.3.1 Slowdown of durotaxis at high stiffness

First, we focus on the decrease of durotactic velocity at high stiffness, which we explain based on the dynamics of the 2D basal cell monolayer. We start by analyzing the role of the friction coefficient ξ. As it increases with substrate stiffness, the durotactic velocity decreases with substrate stiffness. As shown in Fig. S3, the stronger the friction gradient ξ' (Eq. (S18)), the stronger the decay of durotactic velocity at high stiffness.

Next, we analyze the role of force saturation at high stiffnesses. As stiffness increases, active traction forces tend to saturate (Fig. S4a), and hence the traction difference across the tissue, $\Delta\zeta_i \equiv \zeta_i^+ - \zeta_i^-$, decreases (Fig. S5a, for a fixed contact radius R). Because the durotactic velocity increases with the traction difference $\Delta\zeta_i$ (Fig. S5b), traction saturation leads to a decrease of durotactic velocity with stiffness (Fig. S5c). As force saturation is pushed toward higher stiffness by increasing the crossover value E^*, the slowdown of durotaxis is less pronounced (Fig. S4b).

Altogether, both the increase in friction and the saturation of active traction lead to a slower durotaxis at high stiffnesses. Each of these two effects independently slows down durotaxis. Furthermore, both are independent of the 3D shape of the cluster; they arise even in the absence of tissue surface tension as shown in Fig. S5.

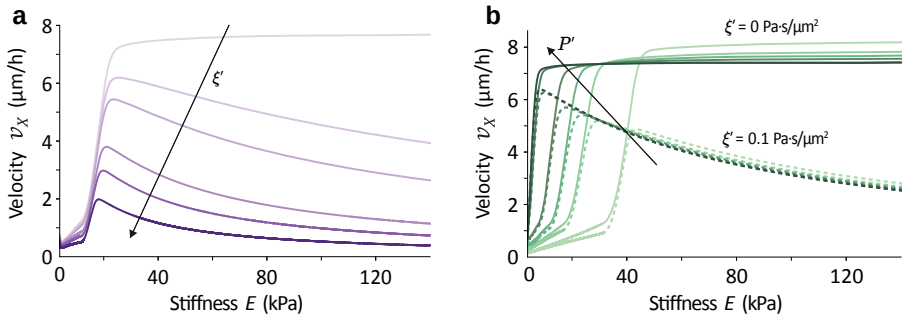

Figure S3. Increasing friction produces a decrease of durotactic velocity with substrate stiffness. Evolution of cluster motion as it moves along a stiffness gradient. The initial shape of the cluster is such with a contact radius $R_0 = 3.0$ μm and height $H_0 = 56.8$ μm, giving $\theta_0 = 174.0°$ (consistent to the experimental measurements of Fig. 1e). Thus, the volume is kept constant to $V = 92500\pi/3$ μm^3. The initial position is $x_0 = 100$ μm ($E_0 = 3.8$ kPa), and we choose linear traction, friction, and pressure profiles (Eqs. (S16) to (S18)) to show that force saturation is not required for the slowdown of durotaxis at high stiffness. **a**, An increasing friction gradient $\xi' = (0, 0.05, 0.1, 0.3, 0.5, 1.0)$ Pa s/μm^2 (from lighter to darker purple), lowers the durotactic velocity at high stiffness. **b**, An increasing pressure gradient $P' = (0.2, 0.4, 0.6, 1.0, 3.0, 4.0)$ Pa/μm (from lighter to darker green), yields smaller contact angles and hence faster durotaxis at low stiffness. However, pressure effects do not produce a velocity decrease at high stiffness; the decrease is only observed when a friction gradient is present (dashed lines). Other parameter values are listed in Table SI except for $\zeta_i^0 = 0.68$ Pa/μm and $\zeta_i' = 0.05$ Pa/μm^2, and the simulation time-step is $\Delta t = 6$ min.

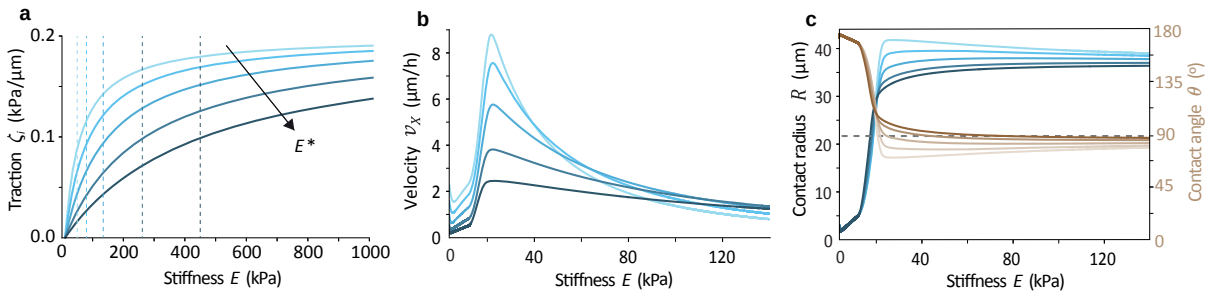

Figure S4. Traction saturation produces a decrease of durotactic velocity with substrate stiffness. a, Active traction profiles against stiffness values, whose saturation shifts to higher stiffness when the crossover stiffness E^* increases (with $E^* = 50, 80, 140, 260, 450$ kPa, from lighter to darker blue). **b-c,** Evolution of cluster motion (**b**) and shape (**c**) as it moves along a stiffness gradient. As E^* increases, the durotactic velocity and contact angle decrease are less pronounced. The initial shape of the cluster is such with a contact radius $R_0 = 3.0$ μm and height $H_0 = 56.8$ μm, giving $\theta_0 = 174.0°$ (consistent to the experimental measurements of Fig. 1e). Thus, the volume is kept constant to $V = 92500\pi/3$ μm^3, and the initial position is $x_0 = 100$ μm ($E_0 = 3.8$ kPa). Other parameter values are listed in Table SI, and the simulation time-step is $\Delta t = 6$ min. The slight increase of the contact angle for large stiffness values (and contact radius decrease), comes from the linear increase of the pressure with stiffness (Eq. (S13)), whereas traction and friction saturate. Thus, the surface tension (which is pointing inwards) is capable of causing monolayer retraction. The effect would be corrected if the pressure also saturated (as for instance in Fig. 3b,c) or decreased its value.

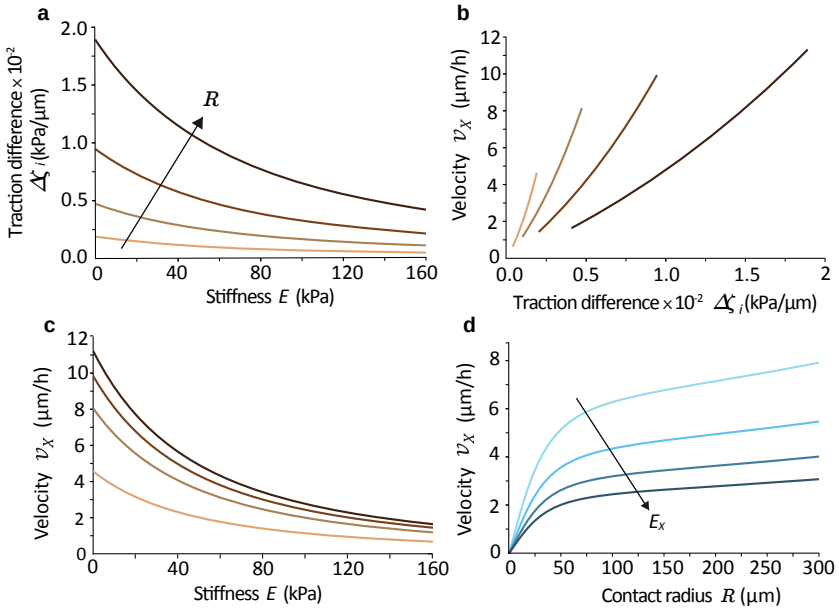

Figure S5. Traction saturation produces a decrease of durotactic velocity with substrate stiffness and an increase with contact radius. The figure corresponds to 2D monolayers, in the absence of tissue surface tension $\gamma = 0$. **a**, Because of traction saturation (Fig. S4a), the active traction difference across the monolayer $\Delta\zeta_i$ decreases with stiffness, but it increases with size R. In panels **a-c**, each curve is for a fixed contact radius R, with values $R = 20, 50, 100, 200$ μm from lighter to darker brown. **b-d**, The durotactic velocity increases with traction difference (**b**), and hence it decreases with stiffness (for a fixed R) (**c,d**). As the active traction difference is larger for larger R, the durotactic velocity increases with contact radius R (for a fixed stiffness value E) (**c,d**). In panel **d**, each curve is for a fixed stiffness, with values $E_X = 25, 50, 75, 100$ kPa from lighter to darker blue. Other parameter values are listed in Table SI.

2.3.2 Speed-up of durotaxis at low stiffness

Now, we focus on the increase of durotactic velocity at low stiffness, which can be explained based on how the 3D shape of the cluster changes with substrate stiffness. To this end, we use our 3D active wetting theory. From the experimental results (Fig. 1e,f), low stiffnesses promote cluster dewetting and hence lead to a high contact angle and low contact radius R. This small R yields a small traction difference across the tissue, which implies a small durotactic velocity (Fig. S5c,d). Increasing the stiffness, the contact angle decreases and so R increases (Fig. S4c and Fig. S6c), producing faster durotaxis. As it affects the contact angle, surface tension γ -and thus pressure P- control the velocity increase, as shown in Fig. S3b and Fig. S6a,b.

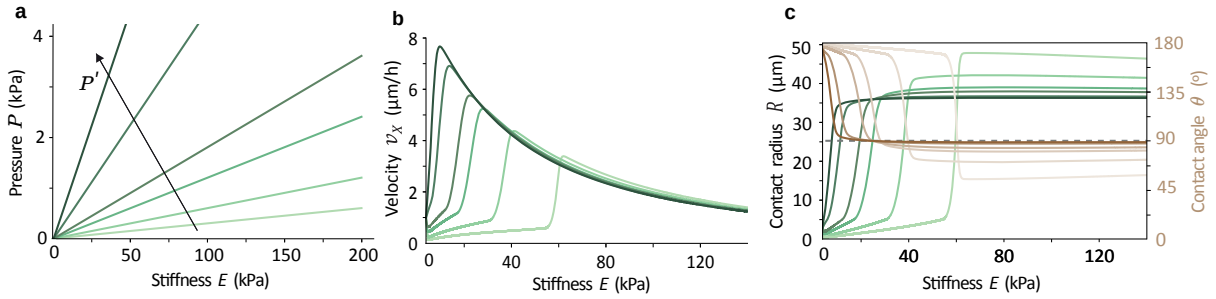

Figure S6. Pressure increase controls the speed-up at low stiffness. a, Pressure profiles against stiffness values, when the pressure gradient increases (with values $P' = (0.1, 0.2, 0.4, 0.6, 1.5, 3.0)$ Pa/μm, from lighter to darker green). **b-c,** Evolution of cluster motion (**b**) and shape (**c**) as it moves along a stiffness gradient. As P' increases, the durotactic velocity and contact radius increase happens sooner, that is, for lower stiffness values. At high stiffnesses, the contact radius saturates and the durotactic velocity decreases due to the two other effects discussed in the text: friction increase (Fig. S3) and traction saturation (Fig. S4). The initial shape of the cluster is such with a contact radius $R_0 = 3.0$ μm and height $H_0 = 56.8$ μm, giving $\theta_0 = 174.0°$ (consistent to the experimental measurements of Fig. 1e). The volume is kept constant to $V = 92500\pi/3$ μm^3, and the initial position is $x_0 = 100$ μm ($E_0 = 3.8$ kPa). Other parameter values are listed in Table SI, and the simulation time-step is $\Delta t = 6$ min.

2.3.3 Dynamic contact angle and location of optimal durotaxis

From the evolution of the clusters along the stiffness gradient, we find that the contact angle never coincides with an equilibrium solution at the corresponding stiffness (Fig. S1). The relaxation toward the equilibrium solution is slow compared to the time scale at which the cluster moves along the stiffness gradient. Accordingly, the observed contact angle is a dynamic one, and the evolution, except for extremely small stiffness gradients, is not quasistatic. Instead, as it performs durotaxis, the cluster has a non-zero spreading velocity, $v_S > 0$. This spreading increases the contact area of the cluster and therefore increases the durotactic velocity.

We see that $v_S(E)$ has a localized peak (blue curve in Fig. 3c and Figs. S9 to S11), which is related to the non-monotonic behavior of $v_S(R)$ in a uniform-stiffness substrate (Fig. S1). This peak gives place to the strongest speedup of the durotactic velocity. When v_S decreases, the durotactic velocity increases more slowly, exhibiting an inflection point close to the location of the v_S peak. Since this region of fast variations is correlated with fast variations of $\cos\theta$, which happen precisely at $\theta = 90°$, the maximal durotactic velocity will be typically near the crossing over 90° of the contact angle. Its exact location along the stiffness axis will depend on details of the profiles of traction and friction vs stiffness, which control the decrease of the durotactic velocity. For the type of profiles discussed here, the maximum of the durotactic velocity is indeed close to the peak of spreading velocity and the crossing over 90° of the contact angle. For extreme (and unrealistic) profiles (for instance for very small friction gradients), the location of maximal durotaxis may in principle depart significantly. Even in such cases though, the maximal values of durotactic velocity do not differ significantly from those reached past the peak of v_S, because the dependence of durotactic velocity with stiffness becomes very flat.

2.4 The durotactic velocity depends on cluster size, cellular contractility, and stiffness gradient

Our experimental results (Fig. 2e,f,g) reveal that the durotactic velocity depends on the cluster size, cell contractility, and stiffness gradient. Here, we show how to capture all these results by modifying the corresponding parameters of our model.

2.4.1 Cluster size

Our experiments show that larger clusters exhibit a higher durotactic velocity, which reaches its maximum at higher substrate stiffness (Fig. 2e). Our model recapitulates these two trends (Fig. 3e and Fig. S7a,d), which we explain in the following way: first, larger clusters have a larger traction difference across them, which drives faster durotaxis (Fig. S5c,d). Second, increasing cluster size favors monolayer wetting [6], and therefore larger clusters have lower contact angles. At low stiffness, the contact angle is always larger than 90°. In this regime, decreasing the contact angle, i.e. making it closer to 90°, implies that the horizontal component of the surface tension becomes smaller (Fig. 3a left). We have previously shown that the horizontal component of surface tension is responsible for the durotactic velocity increase at low stiffness (Fig. 3d, Fig. S6). Thus, larger clusters have a longer increase of durotactic velocity with substrate stiffness, and hence they reach their maximal velocity at higher stiffness.

2.4.2 Cellular contractility

In our experiments, decreasing myosin-generated cellular contractility through the ROCK inhibitor Y-27632 produces slower durotaxis and shifts the maximum of the durotactic velocity toward lower stiffness (Fig. 2f). We recapitulate these trends with our model by decreasing the magnitude of all active forces, i.e. active traction ζ_i, monolayer contractility $|\zeta|$, and tissue surface tension γ (Fig. 3f and Fig. S7b,e). Specifically, we reduce active forces by multiplying their coefficients by factors $\alpha < 1$: $\zeta^{\text{red}} = \alpha_\zeta \zeta$, $\zeta_i^{\text{red}} = \alpha_{\zeta_i} \zeta_i$, $\gamma^{\text{red}} = \alpha_\gamma \gamma$.

Both monolayer contractility ζ and active traction ζ_i are active forces that would vanish completely with no myosin activity. In contrast, tissue surface tension γ has both active and passive contributions [2]. The passive contribution is due to cell-cell adhesion, which would keep cells adhered and thus produce a tissue surface tension even without myosin activity. Therefore, a reduction of myosin activity, as induced by the Y-27632 treatment, affects ζ and ζ_i to a larger extent than γ. To account for this fact, we take $\alpha_\zeta = \alpha_{\zeta_i} < \alpha_\gamma$. Reducing active forces through these factors, we recover the decrease of durotactic velocity and the shift of its maximum toward lower stiffness.

Note that decreasing only the monolayer contractility ζ is not enough to explain the experimental results of the Y-27632 treatment. Decreasing only $|\zeta|$ promotes wetting [6], and therefore it yields higher contact radius (Fig. S8b), shifting the maximal durotactic velocity toward lower stiffness (Fig. S8a). This trend is consistent with the experimental results (Fig. 2f). However, decreasing only $|\zeta|$ also produces faster durotaxis (Fig. S8a), which is opposite to our experimental measurements. Thus, we confirm that to explain the results of the Y-27632 treatment, we need to implement a decrease of all three active forces as explained above.

2.4.3 Stiffness gradient

Finally, our experiments show that a higher stiffness gradient produces faster durotaxis (Fig. 2g). Again, we recapitulate this result with our model (Fig. S7c,f). A higher stiffness gradient implies a larger traction difference across the basal monolayer, which drives faster durotaxis (Fig. S5b). In addition to explaining this result, our predictions reveal that the maximum of the durotactic velocity is shifted toward higher stiffness (Fig. S7c). This shift is due to the fact that a higher stiffness gradient yields a lower contact radius R for a fixed E (Fig. S7f), which we have previously shown to shift the optimal durotactic conditions to stiffer substrates (Fig. S6b,c).

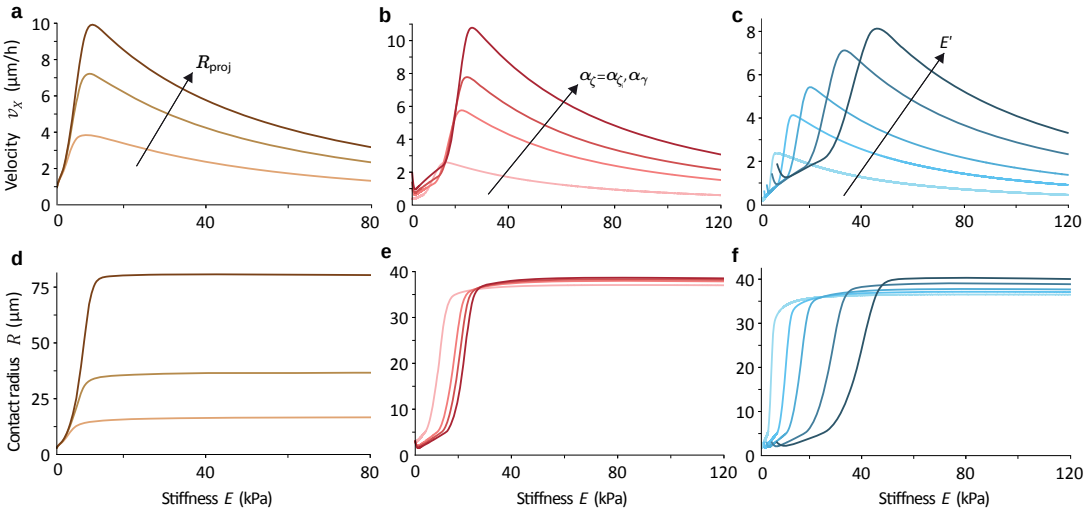

Figure S7. The durotactic velocity depends on cluster size, cellular contractility, and stiffness gradient. Evolution of cluster motion (**a-c**) and contact radius (**d-f**) as it moves along a stiffness gradient. **a**,**d**, Increasing the cluster's volume $V = 9250\pi/3, 92500\pi/3, 925000\pi/3$ µm^3, from lighter to darker brown, leads to larger contact radius (**d**), and hence faster durotaxis (**a**). **b**,**e**, Decreasing all the active forces through factors $\alpha_\zeta = \alpha_{\zeta_i} < \alpha_\gamma$ leads to slower durotaxis and a shift of the velocity maximum to smaller stiffnesses. We take $\alpha_\gamma = 0.7, 1, 1.2, 1.5$ and $\alpha_\zeta = \alpha_{\zeta_i} = 0.4, 1, 1.4, 2$ from lighter to darker red. A stronger decrease in cellular contractility corresponds to smaller α. **c**,**f**, Increasing the stiffness gradient $E' = 10, 20, 30, 50, 70$ kPa/mm from lighter to darker blue, produces an increase of durotactic velocity and a displacement of its peak toward stiffer regions. In all the cases except from the lightest and darkest curves from **a** and **d**, the initial shape of the cluster is such with a contact radius $R_0 = 3.0$ µm and height $H_0 = 56.8$ µm, giving $\theta_0 = 174.0°$ (consistent to the experimental measurements of Fig. 1e). Thus, the volume is kept constant to $V = 92500\pi/3$ µm^3. In the two mentioned exceptions, $R_0 = 3.0$ µm and $H_0 = 26.1, 122.7$ µm, giving $\theta_0 = 166.9°, 177.2°$ respectively, and volume $V = 9250\pi/3, 925000\pi/3$ µm^3. The initial position is $x_0 = 100$ µm ($E_0 = 3.8$ kPa). Other parameter values are listed in Table SI, and the simulation time-step is $\Delta t = 6$ min.

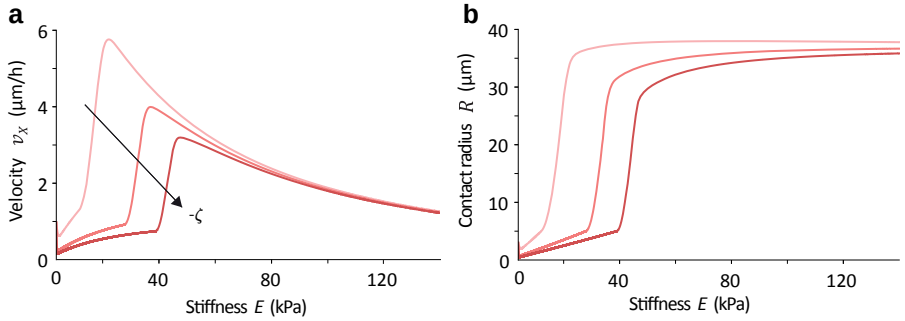

Figure S8. Decreasing only monolayer contractility $|\zeta|$ does not capture the results of the Y-27632 treatment. Evolution of cluster motion (**a**) and contact radius (**b**) as it moves along a stiffness gradient. Increasing monolayer contractility $-\zeta = 2, 5, 7$ kPa from lighter to darker red, produces slower durotaxis and shifts the maximal velocity to higher stiffness (**a**) as it promotes dewetting, i.e. smaller contact radius (**b**). The initial shape of the cluster is such with a contact radius $R_0 = 3.0$ µm and height $H_0 = 56.8$ µm, giving $\theta_0 = 174.0°$ (consistent to the experimental measurements of Fig. 1e). Thus, the volume is kept constant to $V = 92500\pi/3$ µm^3, and the initial position is $x_0 = 100$ µm ($E_0 = 3.8$ kPa). Other parameter values are listed in Table SI, and the simulation time-step is $\Delta t = 6$ min.

2.5 Effects of other parameters in the dynamics of cell cluster durotaxis

Here, we analyze the effects of other parameters in the dynamical evolutions, such as the initial stiffness E_0 (Fig. S9), the contractility $|\zeta|$ (Fig. S10a,b), the pressure offset P_0 (Fig. S10c,d), and the pressure gradient P' (Fig. S11).

We consider a cluster that starts with a high contact angle θ on a soft region of the substrate. As it advances toward stiffer regions, the cluster increases its wettability, lowering its contact angle θ and so expanding its contact radius R. As a result, the cluster increases its durotactic velocity; it speeds up. Eventually, when the cluster reaches sufficiently stiff substrates, the effects of friction increase and traction saturation become more important and the cluster slows down.

However, in many cases, there is an initial decrease of the durotactic velocity, corresponding to a decrease of the contact radius R. This initial slowdown happens when the cluster starts under conditions of dewetting, i.e. with a negative spreading velocity $v_S < 0$. In this situation, the contact radius initially decreases and the contact angle increases, as illustrated in Figs. S9 to S11, in which the initial contact angle is $\theta_0 = 136.4° > 90°$. In a softer initial position (Fig. S9), with higher contractility (Fig. S10a-c), or with smaller values of the pressure and thus the surface tension (Fig. S11), this early-stage effect is accentuated, since all these parameters favor cluster dewetting. Instead, a larger pressure diminishes this effect because it favors the expansion of R at the initial stages and when $\theta > 90°$.

Finally, if the pressure does not increase with stiffness (Fig. S10d,e), surface tension offers a lower opposition to cluster spreading in low contact angle conditions ($\theta < 90°$). As a result, the contact radius keeps increasing significantly even at high stiffness). Nevertheless, the durotactic velocity still decreases due to the increase of friction forces.

Observing and characterizing this full spectrum of dynamical evolutions in experiments remains a challenge for future work.

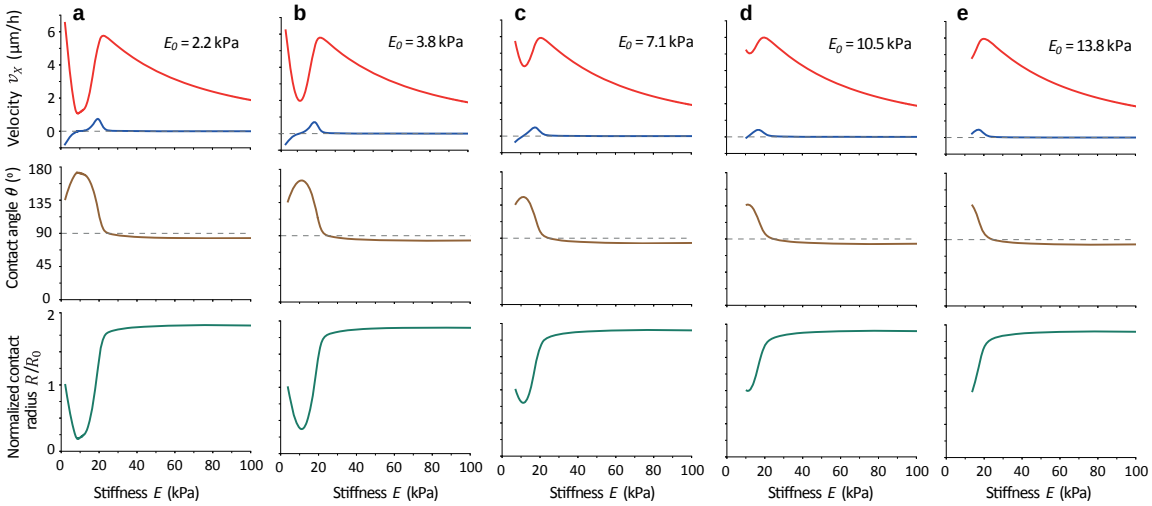

Figure S9. Dynamics of cluster durotaxis when varying the initial substrate stiffness. Evolution of cluster motion and shape as it moves along a stiffness gradient, with saturated traction and friction and linear pressure profiles. Regarding the velocity plots, the durotactic velocity is in red and the spreading velocity in blue. At each case, the initial shape of the cluster is such with a contact radius $R_0 = 20.0$ μm and height $H_0 = 50.0$ μm, giving $\theta_0 = 136.4°$ and a constant volume $V = 92500\pi/3$ μm^3. We change the initial position to $x_0 = 50, 100, 200, 300, 400$ μm, corresponding to $E_0 = 2.2, 3.8, 7.1, 10.5, 13.8$ kPa. Other parameter values are listed in Table SI, and the simulation time-step is $\Delta t = 6$ min.

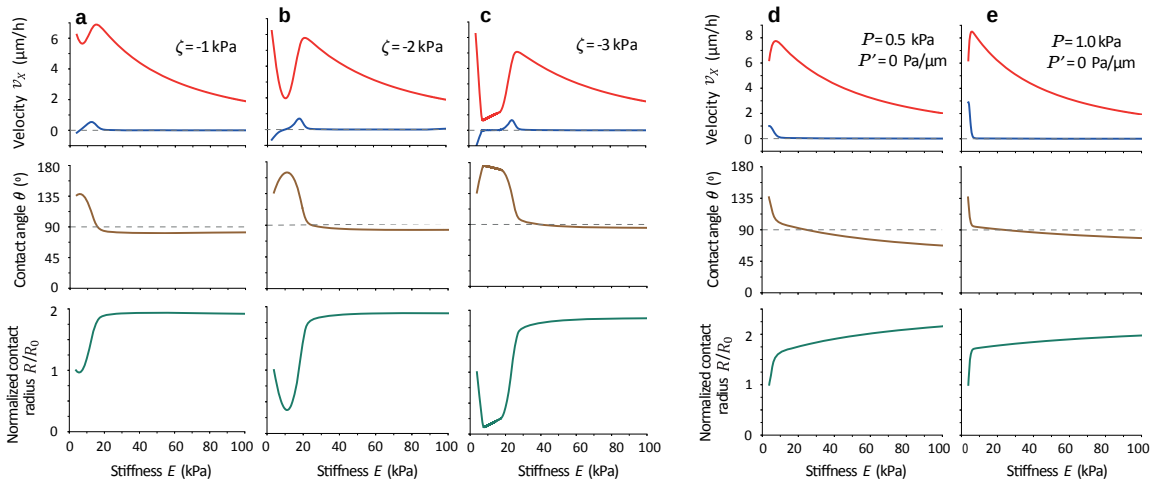

Figure S10. Dynamics of cluster durotaxis when varying the contractility and pressure. Evolution of cluster motion and shape as it moves along a stiffness gradient, with saturated traction and friction and linear pressure profiles. Regarding the velocity plots, the durotactic velocity is in red and the spreading velocity in blue. At each case, the initial shape of the cluster is such with a contact radius $R_0 = 20.0$ μm and height $H_0 = 50.0$ μm, giving $\theta_0 = 136.4^\circ$ and a constant volume $V = 92500\pi/3$ μm^3. The initial position is $x_0 = 100$ μm ($E_0 = 3.8$ kPa). In **a-c** we change the contractility to $-\zeta = 1, 2, 3$ kPa, with a linear pressure profile $P_{0x} = 4.2$ Pa and $P' = 0.6$ Pa/μm. In **d** and **e**, we take a uniform pressure of $P = 0.5$ and 1.0 kPa respectively, with a fixed contractility $\zeta = -2$ kPa. Other parameter values are listed in Table SI, and the simulation time-step is $\Delta t = 6$ min.

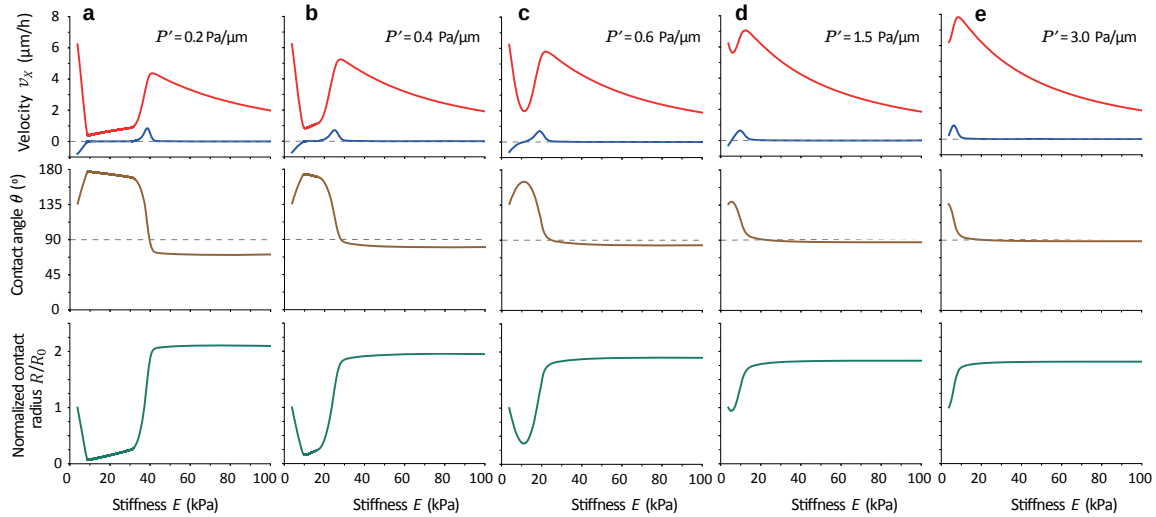

Figure S11. Dynamics of cluster durotaxis when varying the pressure gradient. Evolution of cluster motion and shape as it moves along a stiffness gradient, with saturated traction and friction and linear pressure profiles. Regarding the velocity plots, the durotactic velocity is in red and the spreading velocity in blue. At each case, the initial shape of the cluster is such with a contact radius $R_0 = 20.0$ μm and height $H_0 = 50.0$ μm, giving $\theta_0 = 136.4^\circ$ and a constant volume $V = 92500\pi/3$ μm^3. The initial position is $x_0 = 100$ μm ($E_0 = 3.8$ kPa), and we change the pressure gradient to $P' = (0.2, 0.4, 0.6, 1.5, 3.0)$ Pa/μm. Other parameter values are listed in Table SI, and the simulation time-step is $\Delta t = 6$ min.

References

1. Lecuit, T. & Lenne, P. F. Cell surface mechanics and the control of cell shape, tissue patterns and morphogenesis. *Nat. Rev. Mol. Cell Biol.* **8,** 633–644 (2007).
2. Manning, M. L., Foty, R. A., Steinberg, M. S. & Schoetz, E.-M. Coaction of intercellular adhesion and cortical tension specifies tissue surface tension. *PNAS* **107,** 12517–12522 (2010).
3. Guevorkian, K., Colbert, M. J., Durth, M., Dufour, S. & Brochard-Wyart, F. Aspiration of biological viscoelastic drops. *Phys. Rev. Lett.* **104,** 218101 (2010).
4. Maître, J. L. & Heisenberg, C. P. The role of adhesion energy in controlling cell-cell contacts. *Curr. Opin. Cell Biol.* **23,** 508–514 (2011).
5. Ehrig, S. *et al.* Surface tension determines tissue shape and growth kinetics. *Sci. Adv.* **5,** 9394–9405 (2019).
6. Active wetting of epithelial tissues. *Nat. Phys.* **15,** 79–88 (2019).
7. Walcott, S. & Sun, S. X. A mechanical model of actin stress fiber formation and substrate elasticity sensing in adherent cells. *PNAS* **107,** 7757–7762 (2010).
8. Saez, A. *et al.* Traction forces exerted by epithelial cell sheets. *J. Phys.: Condens. Matter* **22,** 194119 (2010).
9. Trichet, L. *et al.* Evidence of a large-scale mechanosensing mechanism for cellular adaptation to substrate stiffness. *PNAS* **109,** 6933–6938 (2012).
10. Gupta, M. *et al.* Adaptive rheology and ordering of cell cytoskeleton govern matrix rigidity sensing. *Nat. Commun.* **6,** 7525 (2015).
11. Marcq, P., Yoshinaga, N. & Prost, J. Rigidity sensing explained by active matter theory. *Biophys. J.* **101,** L33–L35 (2011).
12. Sens, P. Rigidity sensing by stochastic sliding friction. *Europhys. Lett.* **104,** 38003 (2013).
13. Alert, R., Blanch-Mercader, C. & Casademunt, J. Active Fingering Instability in Tissue Spreading. *Phys. Rev. Lett.* **122,** 088104 (2019).
14. Alert, R. & Casademunt, J. Role of Substrate Stiffness in Tissue Spreading: Wetting Transition and Tissue Durotaxis. *Langmuir* **35,** 7571–7577 (2019).
15. Pi-Jaumà, I., Alert, R. & Casademunt, J. Collective durotaxis of cohesive cell clusters on a stiffness gradient. *Eur. Phys. J. E* **45,** 7 (2022).
16. Weber, G. F., Bjerke, M. A. & DeSimone, D. W. A Mechanoresponsive Cadherin-Keratin Complex Directs Polarized Protrusive Behavior and Collective Cell Migration. *Dev. Cell* **22,** 104–115 (2012).
17. Smeets, B. *et al.* Emergent structures and dynamics of cell colonies by contact inhibition of locomotion. *PNAS* **113,** 14621–14626 (2016).
18. Blanch-Mercader, C. *et al.* Effective viscosity and dynamics of spreading epithelia: a solvable model. *Soft Matter* **13,** 1235–1243 (2017).
19. Vincent, R. *et al.* Active Tensile Modulus of an Epithelial Monolayer. *Phys. Rev. Lett.* **115,** 248103 (2015).
20. De Gennes, P.-G. & Prost, J. *The Physics of Liquid Crystals* (Oxford, UK: Oxford Univ. Press. 2nd ed, 1993).
21. Alert, R. & Trepat, X. Physical Models of Collective Cell Migration. *Annu. Rev. Condens. Matter Phys.* **11,** 77–101 (2020).
22. Kruse, K., Joanny, J. F., Jülicher, F., Prost, J. & Sekimoto, K. Generic theory of active polar gels: A paradigm for cytoskeletal dynamics. *Eur. Phys. J. E* **16,** 5–16 (2005).
23. Jülicher, F., Kruse, K., Prost, J. & Joanny, J. F. Active behavior of the Cytoskeleton. *Phys. Rep.* **449,** 3–28 (2007).
24. Marchetti, M. *et al.* Hydrodynamics of soft active matter. *Rev. Mod. Phys.* **85,** 1143–1189 (2013).

25. Prost, J., Jülicher, F. & Joanny, J. F. Active gel physics. *Nat. Phys.* **11,** 111–117 (2015).

26. Jülicher, F., Grill, S. W. & Salbreux, G. Hydrodynamic theory of active matter. *Rep. Prog. Phys.* **81,** 076601 (2018).

27. Oriola, D., Alert, R. & Casademunt, J. Fluidization and Active Thinning by Molecular Kinetics in Active Gels. *Phys. Rev. Lett.* **118,** 088002 (2017).

28. Sunyer, R. *et al.* Collective cell durotaxis emerges from long-range intercellular force transmission. *Science* **353,** 1157–1161 (2016).

29. Ryan, P. L., Foty, R. A., Kohn, J. & Steinberg, M. S. Tissue spreading on implantable substrates is a competitive outcome of cell-cell vs. cell-substratum adhesivity. *PNAS* **98,** 4323–4327 (2001).

30. Douezan, S. *et al.* Spreading dynamics and wetting transition of cellular aggregates. *PNAS* **108,** 7315–7320 (2011).

31. Douezan, S., Dumond, J. & Brochard-Wyart, F. Wetting transitions of cellular aggregates induced by substrate rigidity. en. *Soft Matter* **8,** 4578–4583 (2012).

32. Beaune, G. *et al.* How cells flow in the spreading of cellular aggregates. *PNAS* **111,** 8055–8060 (2014).

33. Trepat, X. *et al.* Physical forces during collective cell migration. *Nat. Phys.* **5,** 426–430 (2009).

34. Cochet-Escartin, O., Ranft, J., Silberzan, P. & Marcq, P. Border forces and friction control epithelial closure dynamics. *Biophys. J.* **106,** 65–73 (2014).